

Research Article

Petrogenesis of the Triassic granitoids from the East Kunlun Orogenic Belt, NW China: Implications for continental crust growth from syn-collisional to post-collisional setting



Juanjuan Kong ^{a,b,*}, Yaoling Niu ^{b,c,d,*}, Yan Hu ^e, Yu Zhang ^b, Fengli Shao ^f

^a College of Ocean Science and Engineering, Shandong University of Science and Technology, Qingdao 266590, China

^b Laboratory for Marine Geology, Qingdao National Laboratory for Marine Science and Technology, Qingdao 266061, China

^c Department of Earth Sciences, Durham University, Durham DH1 3LE, UK

^d State Key Laboratory of Geological Processes and Mineral Resources, and School of Earth Science and Mineral Resources, China University of Geosciences, Beijing 100083, China

^e Geological Survey Institute of Gansu Province, Lanzhou 730000, China

^f Linyi University, Linyi 276000, China

ARTICLE INFO

Article history:

Received 7 November 2019

Received in revised form 20 March 2020

Accepted 25 March 2020

Available online 05 April 2020

Keywords:

East Kunlun Orogenic Belt
Syn-collisional granitoids
Post-collisional granitoids
Continental crust growth
A'nyemaqen Ocean

ABSTRACT

The Triassic granitoids are widespread in the eastern section of the East Kunlun Orogenic Belt (EKOB) on the northern Tibetan Plateau. These granitoids well record the evolution of the Paleo-Tethys oceans (named as A'nyemaqen Ocean in the EKOB). Our new zircon U–Pb data together with ages in literature show that these granitoids represent long-lasting magmatism from the early (T_1 , ~251–248 Ma), middle (T_2 , ~247–238 Ma) to late (T_3 , ~234–214 Ma) Triassic. The Triassic granitoids display calc-alkaline I-type granite affinities and hybrid mantle-crust geochemical signatures. The T_1 granitoids possess andesitic to felsic bulk continental crust (BCC)-like chemical composition (e.g., enriched in Rb, K and Pb, depleted in Nb, Ta, Sr, P and Ti), coupled with high I_{Sr} (0.7067–0.7148), negative $\varepsilon_{Nd(t)}$ (−7.32 to −1.66) and negative to positive $\varepsilon_{Hf(t)}$ (−5.11 to 3.59) as well as $(Dy/Yb)_N = 1.1$, suggesting that the T_1 granitoids were formed by melting of the subducted A'nyemaqen oceanic crust with terrigenous sediments under the amphibolite facies conditions in a syn-collisional setting. The T_2 and T_3 granitoids may be originated from a relatively homogeneous source with almost consistent mean values of I_{Sr} (0.7136 [T_2], 0.7094 [T_3]), $\varepsilon_{Nd(t)}$ (−5.83 [T_2], −5.97 [T_3]) and $\varepsilon_{Hf(t)}$ (−3.52 [T_2], −3.58 [T_3])). They present garnet signature of adakitic rocks and can be explained by partial melting of the juvenile mafic lower continental crust and mixing with upper crustal components during magma ascent. This process is considered to be associated with post-collisional extension which induced by asthenosphere upwelling and mantle melting, providing heat for mafic lower crust melting to form T_2 and T_3 granitoids. The T_1 granitoids with mantle signatures (e.g. $\varepsilon_{Hf(t)} > 0$) as well as BCC-like compositions represent a net flux of juvenile dioritic to granitic materials adding to the continental crust, in support of the hypothesis of “continental collision zones are primary sites for net continental crust growth” along the EKOB. The genetic link between T_2 and T_3 granitoids means the EKOB had transformed to post-collisional setting since the middle Triassic (~247 Ma). All these hypotheses are conceptually important for understanding the origin of the juvenile crust and continental crustal growth through magmatism from syn-collisional to post-collisional settings.

© 2020 Elsevier B.V. All rights reserved.

1. Introduction

Granitoid batholiths are the most abundant constituent of continental crust, and their origin is essential for understanding the evolution and differentiation of the continental crust (Luo et al., 2015). The East Kunlun Orogenic Belt (EKOB) as one of the major magmatic belts on the Tibetan Plateau is considered to undergo multi-cycle tectonic

evolution and record the evolution of the Proto- and Paleo-Tethys oceans from the Early Paleozoic to the Early Mesozoic (Mo et al., 2007; Xiong et al., 2014). Widespread granitoid batholiths of two episodes, i.e. Early Paleozoic and Late Paleozoic-Triassic in the EKOB formed in volcanic-arc, syn-collisional and post-collisional settings have supplied much information to help understand the geological evolution of the Proto- and Paleo-Tethys oceans over the past three decades (Huang et al., 2014; Jiang et al., 1992; Shao et al., 2017). We focus on the Triassic granitoids in the eastern section of the EKOB where previous studies have revealed the history of Paleo-Tethys orogenic events of 270–195 Ma (Chen et al., 2007; Sun et al., 2009; Xiong et al., 2012;

* Corresponding authors.

E-mail addresses: juanjuan0317@foxmail.com (J. Kong), [\(Y. Niu\).](mailto:yaoling.niu@durham.ac.uk)

Zhang et al., 2012; Xu et al., 2015). Despite the large number of recent studies on the tectonic evolution of the Paleo-Tethys, many uncertainties and controversies remain (Mo et al., 2007; Pan et al., 2012; Xia et al., 2015). Moreover, these studies concentrated on scattered/individual intrusions, lacking systemic chronology, geochemistry, and especially isotopic investigations.

Continental crustal growth is widely considered to be associated with the subduction-zone magmatism because of the arc-like incompatible element signature of the bulk continental crust (BCC) (e.g., enrichment in U, K and Pb, depletion in Nb, Ta and Ti; Niu et al., 2013), which is termed “island arc model” (Taylor, 1967). However, the standard “island arc model” has many difficulties (Niu et al., 2013; Niu and O’Hara, 2009), aiming at which Niu and co-workers proposed a testable hypothesis “continental collision zones are primary sites of net continental crustal growth”. Because of this and on the basis of

their detailed studies of the Linzizong syncollisional volcanic sequence in southern Tibet (Mo et al., 2008), this hypothesis has been tested with success in several orogenic belts (Huang et al., 2014; Kong et al., 2017; Mo et al., 2008; Niu et al., 2013; Niu and O’Hara, 2009; Shao et al., 2017; Zhang et al., 2016), including the preliminary study of the EKOB syn-collisional granitoids. Furthermore, comparison between the syn- and post-collisional granitoids in the Triassic offers important information for the continental crust growth in different context of the orogenesis.

In this paper, we systematically present new geochemical and geochronological data for the granitoids in the eastern section of the EKOB. Our new data, together with age data from the literature, shed light on the petrogenesis of the granitoids from the syn- to post-collisional settings and provide constraints on the evolution of the Paleo-Tethys oceans and continental crustal growth in the EKOB.

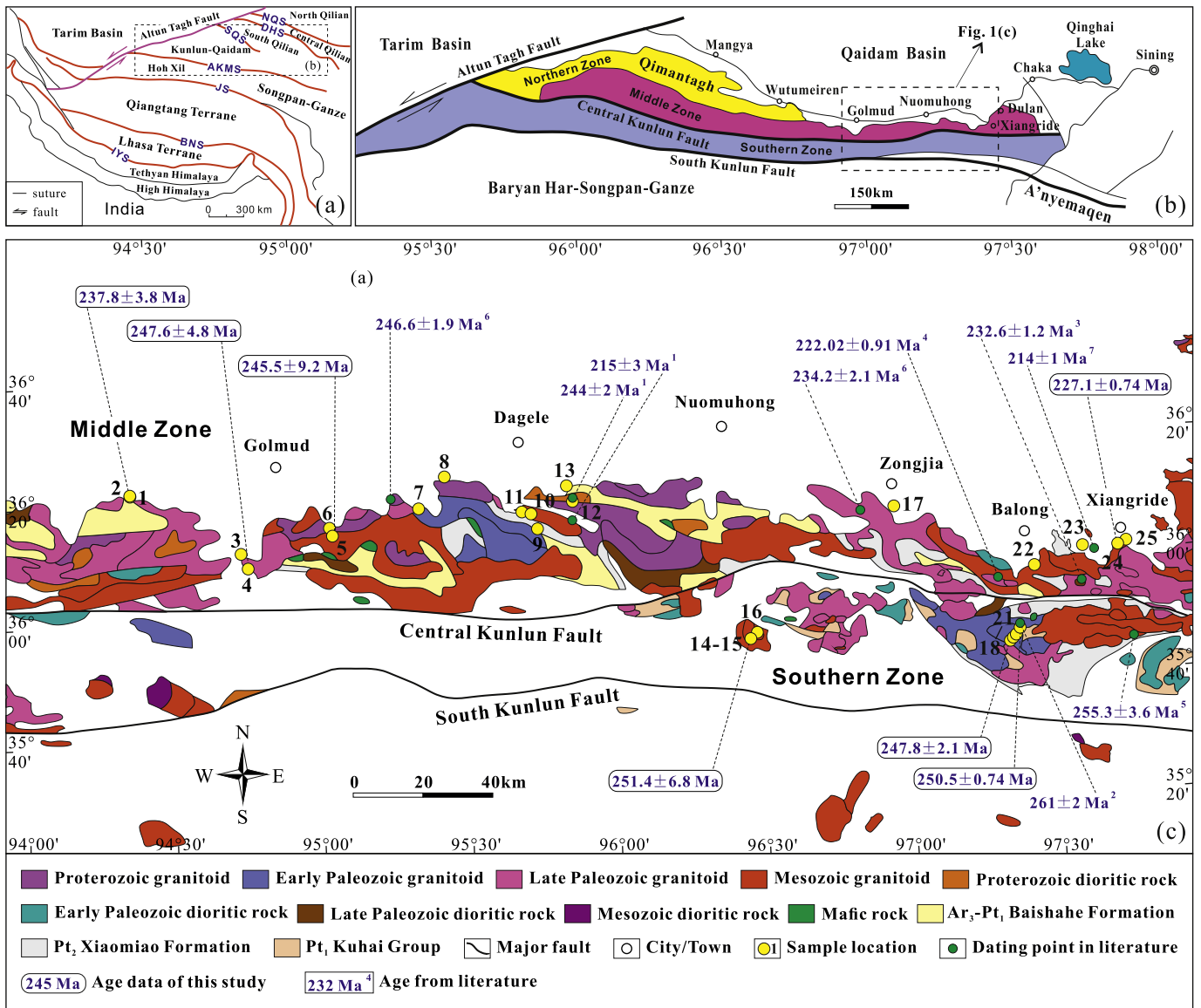


Fig. 1. (a) Geological framework of the Greater Tibetan Plateau showing the major tectonic units and sutures as follows (from northeast to southwest): NQS, North Qilian suture; DHS, Danghe Nan Shan suture; SQS, South Qilian suture; AKMS, A'nyemagen-Kunlun-Mutztagh suture; JS, Jinsha suture; BNS, Bangong-Nujiang suture; IYS, Indus-Yarlung Zangbo suture, revised after (Hu et al., 2016). (b) Outline of the East Kunlun Orogenic Belt with two major faults (Central Kunlun Fault and South Kunlun Fault) and three magmatic zones (Northern, Middle and Southern Zone) (Hu et al., 2016). (c) Simplified geological map of east section of the East Kunlun Orogenic Belt (modified after XACGS, 2009). U-Pb ages shown for the granitic plutons are new data of this study and from the recent literature indicated with superscript numerals: 1. Ding et al. (2014), 2. Xiong et al. (2012), 3. Xia et al. (2014a), 4. Xia et al. (2014b), 5. Sun et al. (2009), 6. Xu et al. (2015) and 7. Ding et al. (2011).

2. Geological setting and samples

The EKOB is located south of the Kunlun-Qaidam terrane constrained between the south Qilian suture (SQS) to the north and the A'nyemaqen-Kunlun-Mutztagh suture (AKMS) in the south on the northern Tibet Plateau. The globally unique Tibetan Plateau has been amalgamated through multiple continental collision events, resulting in progressively younger sutures from northeast (Early Paleozoic) to southwest (Cenozoic) (Fig. 1a; Niu et al., 2013). The northern Tibet Plateau is thus the ideal site for studying the processes of continental collision and geological consequences. The EKOB is bounded by the Qaidam Basin to the north and Baryan Har-Songpan Ganze terrane (BH-SG) to the south, extending W-E for ~1500 km (Fig. 1b; Jiang et al., 1992; Ding et al., 2014). Three sub-units (the northern, middle and southern zone) have been recognized in the EKOB, separated by two subparallel faults (Central and South Kunlun Fault) offset by the Altun Tagh sinistral strike-slip fault in the west (Fig. 1b; Jiang et al., 1992; Liu et al., 2004). Our study area is in the eastern section of the EKOB with middle and southern magmatic zones well exposed. The middle zone is dominated by Late Paleozoic and Triassic granitoids. It also contains Precambrian metamorphic basement, Devonian sandstones, conglomerates and Carboniferous marine limestones and clastic sedimentary rocks. Comparatively, the southern zone is a more

complex fold belt, which is divided into western Late Paleozoic fold group, middle Precambrian uplift and eastern Paleozoic and Triassic fold group. The basement is dominated by the Mesoarchean-Mesoproterozoic Jinshukou Group in the middle zone and the Paleoproterozoic Kuhai Group in the southern zone (Fig. 1c). The Jinshukou Group, which comprises the lower Mesoarchean-Paleoproterozoic Baishahe Formation and the upper Mesoproterozoic Xiaomiao Formation (Chen et al., 2011; Wang et al., 2004). The Jinshukou Group is consist of gneisses, marbles, greenschists, amphibolites, migmatites and quartzites and had been involved into later granulite-facies metamorphism and anatexis during 460–402 Ma (Zhang et al., 2003; Wang et al., 2007). The Kuhai Group is a metamorphic rock series of amphibolite facies forming during 2330–1441 Ma, which consist of gneiss, plagioclase amphibolite, quartz schist and migmatites (Wang et al., 2007). Two ophiolite belts distributed along the Central and South Kunlun Fault, the Nuomuhong-Qingshuiquan ophiolite belt (NQO) extending along the south of the Central Kunlun Fault and the A'nyemaqen ophiolite belt (AMO) in the southern margin of the EKOB (Bian et al., 2001; Jiang et al., 1992; Zhang et al., 2012). It is accepted that the NQO formed in the Early Paleozoic, indicating the closure of Central Kunlun Ocean (Yang et al., 1996; Li et al., 2012). While the formation age of the AMO is relatively complex. Many studies have confirmed that the AMO represent two stages of ocean closing, i.e. Early

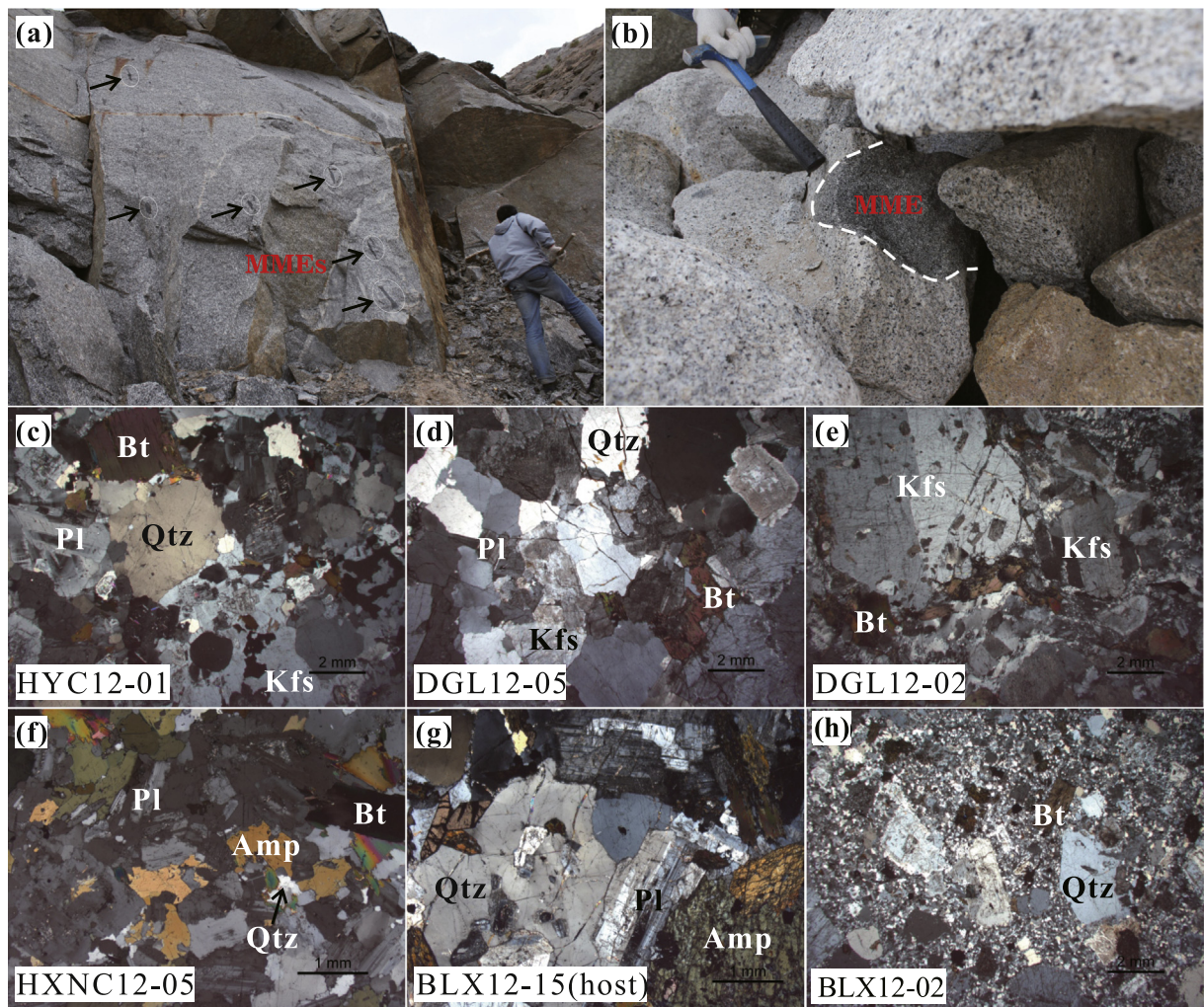


Fig. 2. (a, b) An outcrop of the Triassic granitoids with some mafic magmatic enclaves (MMEs) from the East Kunlun Orogenic Belt. Photomicrographs of (c) biotite monzogranite, (d) syenogranite, (e) biotite moyite, (f) quartz diorite, (g) granodiorite, (h) granite porphyry. Kfs = potash feldspar; Qtz = quartz; Pl = plagioclase; Bt = biotite; Amp = amphibole.

Paleozoic (~467 Ma) Qinling-Qilian-Kunlun Ocean (Bian et al., 2004); Late Paleozoic to Middle Triassic (~308–260 Ma) Paleo-Tethys Ocean (Jiang et al., 1992; Yang et al., 2009).

The EKOB preserves geological records of the Early Paleozoic Caledonian cycles and the Late Paleozoic to Early Mesozoic Variscan-Indosinian cycle. The Early Paleozoic (500–400 Ma) granitoids are comparable with those in the North Qilian orogenic belt (Mo et al., 2007). The Permian-Triassic granitoids are dominant in the EKOB (~25,000 km²) and account for 50% of the total outcrop area of the granitoids (Fig. 1c, Jiang et al., 1992; Zhang et al., 2014).

Samples of this study are collected from the eastern section of the EKOB, which extend W-E for ~300 km and distribute in the Middle and Southern Zones (Fig. 1c). They are intermediate- to coarse-grained granites to granodiorites (Fig. 2) with mineral assemblage of quartz + potash feldspar + plagioclase + amphibole + biotite + magnetite and accessory minerals of apatite and zircon (see Table 1 for detail). Fine-grained dioritic mafic magmatic enclaves (MMEs) are dispersed in the pluton (Fig. 2a, b).

3. Analytical methods

3.1. Zircon U-Pb dating

Zircons from seven samples were separated for U-Pb dating using combined methods of heavy liquid and magnetic techniques. The zircon internal structure was examined using cathodoluminescence (CL) imaging on a FEI Quanta 450 FEG scanning electron microscope (SEM) at the State Key Laboratory of Geological Processes and Mineral Resources (GPMR), China University of Geosciences, Wuhan. U-Pb dating was

conducted by laser ablation inductively coupled plasma mass spectrometry (LA-ICP-MS) at the same laboratory, using a 32 μm spot size. Zircon 91,500 was used as the external standard (Wiedenbeck et al., 1995). Each block of 6 unknowns was bracketed by analyses of the standards. Off-line selection and integration of background and analyte signals, and time-drift correction and quantitative calibration for trace element analyses and U-Pb dating were performed by ICP-MS-Data-Cal (Liu et al., 2010). Eighteen points of each sample were chosen for LA-ICP-MS U-Pb analysis and their results are given in Appendix A. Concordia diagrams and weighted mean calculations were processed using the Isoplot/Ex_version 4.15 program (Ludwig, 2012). Concordia diagrams and representative CL images of seven samples are shown in Fig. 3.

3.2. Major and trace elements

Twenty-five freshest samples were chosen for elemental analysis. Weathered surfaces and pen saw marks were removed, cleaned, and ultrasonically cleaned with Milli-Q water and dried before powdered using an agate mill into ~200-mesh in a clean environment.

Major elements were determined using a Leeman Prodigy inductively coupled plasma-optical emission spectroscopy (ICP-OES) system with high dispersion Echelle optics at China University of Geosciences, Beijing (CUGB). The precision (1σ) based on rock standards BCR-1, AGV-2 and GSR-3 is estimated as ~1.5% for TiO₂, ~2.0% for P₂O₅ and better than 1% for other major oxides. And trace elements were analyzed using an Agilent-7500a inductively coupled plasma mass spectrometry (ICP-MS) at CUGB. The BCR-1 and BHVO-1 were used to calibrate the elemental concentrations of the samples. The analytical precision was generally better than 5% for most trace elements, 10–13% for Cu, Sc,

Table 1

Sample locations and zircon U-Pb ages of the Triassic granitoids in the East Kunlun Orogenic Belt.

Sample	Point	GPS	Lithology	Petrology	Age (Ma)
AKDL12-01	14	N35°50'28.3"	E96°29'26.2"	syenogranite	Kfs (45%), Qtz (27%), Pl (15%), Mag (8%), Bt (5%); Kfs with kaolinization.
AKDL12-03	15	N35°50'28.2"	E96°29'32.1"	moyite	Kfs (50%), Qtz (30%), Mag (7%), Amp (5%), Bt (4%), Pl (4%).
AKDL12-04	16	N35°51'27.3"	E96°31'5.2"	moyite	Kfs (55%), Qtz (30%), Pl (5%), Mag (5%), Bt (5%).
BLX12-09	21	N35°48'34.9"	E97°24'25.8"	granodiorite	Pl (50%), Qtz (20%), Bt (10%), Amp (5%); accessory mineral (Ap)
BLX12-03	18	N35°46'38.5"	E97°22'11.2"	monzogranite	Qtz (35%), Kfs (30%), Pl (25%), Bt (10%); Kfs with kaolinization.
BLX12-06	19	N35°46'58.9"	E97°22'51.1"	granite porphyry	Phenocrysts of Qtz (40%), Kfs (30%), Pl (25%), Bt (5%), Qtz and Kfs with melt corrosion shapes; groundmass with the same mineral assemblage.
BLX12-08	20	N35°47'37.2"	E97°23'43.0"	monzogranite	Qtz (30%), Kfs (30%), Pl (25%), Bt + Mag (15%).
HXNC12-07	3	N36°18'53.8"	E94°35'21.4"	granite	Qtz (40%), Pl (35%), Kfs (10%), Bt (10%), Mag (5%); accessory minerals (Ap + Zrn); Pl with sericitization.
NSK12-09	4	N36°8'14.6"	E94°47'57.7"	syenogranite	Kfs (45%), Qtz (28%), Pl (15%), Bt (8%), Mag (4%); Kfs with kaolinization.
GYK12-05	7	N36°16'19.3"	E95°23'56.6"	biotite granite	Qtz (35%), Pl (30%), Kfs (15%), Bt (20%).
DGLX12-01	8	N36°21'23.1"	E95°29'25"	granodiorite	Pl (35%), Qtz (25%), Kfs (10%), Bt + Amp + Mag (30%).
DGL12-01	9	N36°11'33.5"	E95°47'39.2"	biotite granite	Qtz (30%), Pl + Kfs (45%), Bt (20%), Mag (5%).
DGL12-02	9	N36°11'33.5"	E95°47'39.2"	biotite moyite	Kfs (45%), Qtz (30%), Bt (25%); porphyroid texture.
HYC12-01	5	N36°12'55"	E95°05'36"	biotite	Qtz (30%), Kfs (30%), Pl (30%), Bt (10%).
HYC12-06	6	N36°14'6.3"	E95°05'6.8"	monzogranite	Qtz (28%), Pl (35%), Kfs (15%), Bt (20%), Amp (2%).
(host)					
WLG12-05	12	N36°15'40.5"	E95°55'12.2"	syenogranite	Kfs (50%), Qtz (30%), Pl (10%), Chl (10%).
WLG12-07	13	N36°18'17"	E95°54'11.4"	syenogranite	Kfs (40%), Qtz (30%), Pl (15%), Bt (15%); accessory mineral (Zrn)
HXNC12-01	1	N36°21'31.4"	E94°24'37.6"	syenogranite	Kfs (48%), Qtz (32%), Pl (10%), Bt (10%).
HXNC12-05	2	N36°21'39.8"	E94°24'37.8"	quartz diorite	Pl (40%), Qtz (20%), Bt + Amp (40%).
ZJX12-01	17	N36°10'27.8"	E97°01'10.6"	quartz diorite	Pl (40%), Qtz (10%), Kfs (10%), Bt + Amp (35%), Mag (5%).
BLXD12-06	24	N36°01'8.7"	E97°46'17"	amphibole quartz monzonite	Kfs (30%), Pl (30%), Qtz (15%), Bt + Amp (25%).
WLS12-01	25	N36°01'33.5"	E97°48'7.3"	syenogranite	Kfs (50%), Qtz (30%), Pl (12%), Bt (5%), Mag (3%).
BLX12-15	22	N35°58'39.6"	E97°28'32.1"	granodiorite	Pl (45%), Qtz (25%), Kfs (5%), Bt + Amp (20%); Mag (5%).
(host)					
DGL12-05	10	N36°14'4.3"	E95°46'35.7"	syenogranite	Kfs (57%), Qtz (30%), Pl (8%), Bt (5%).
DGL12-07	11	N36°14'28"	E95°44'47.6"	moyite	Kfs (56%), Qtz (28%), Bt (8%), Pl (5%), Mag (3%).
BLXD12-02	23	N36°01'34.3"	E97°39'4.1"	granite porphyry	Phenocrysts of Qtz and feldspar, Qtz and feldspar with melt corrosion shapes; groundmass of Kfs (50%), Qtz (30%), Bt (10%), Pl (5%), Mag (5%).

Kfs = potash feldspar; Qtz = quartz; Pl = plagioclase; Bt = biotite; Amp = amphibole; Mag = magnetite; Ap = apatite; Zrn = zircon.

Ages with superscript are from literature being the same as that in Fig. 1.

215 ± 3¹

215 ± 3¹

214 ± 1⁷

227.1 ± 0.74

222.02 ± 0.91⁴

244 ± 2¹

244 ± 2¹

237.8 ± 3.8

237.8 ± 3.8

234.2 ± 2.1⁶

227.1 ± 0.74

227.1 ± 0.74

222.02 ± 0.91⁴

215 ± 3¹

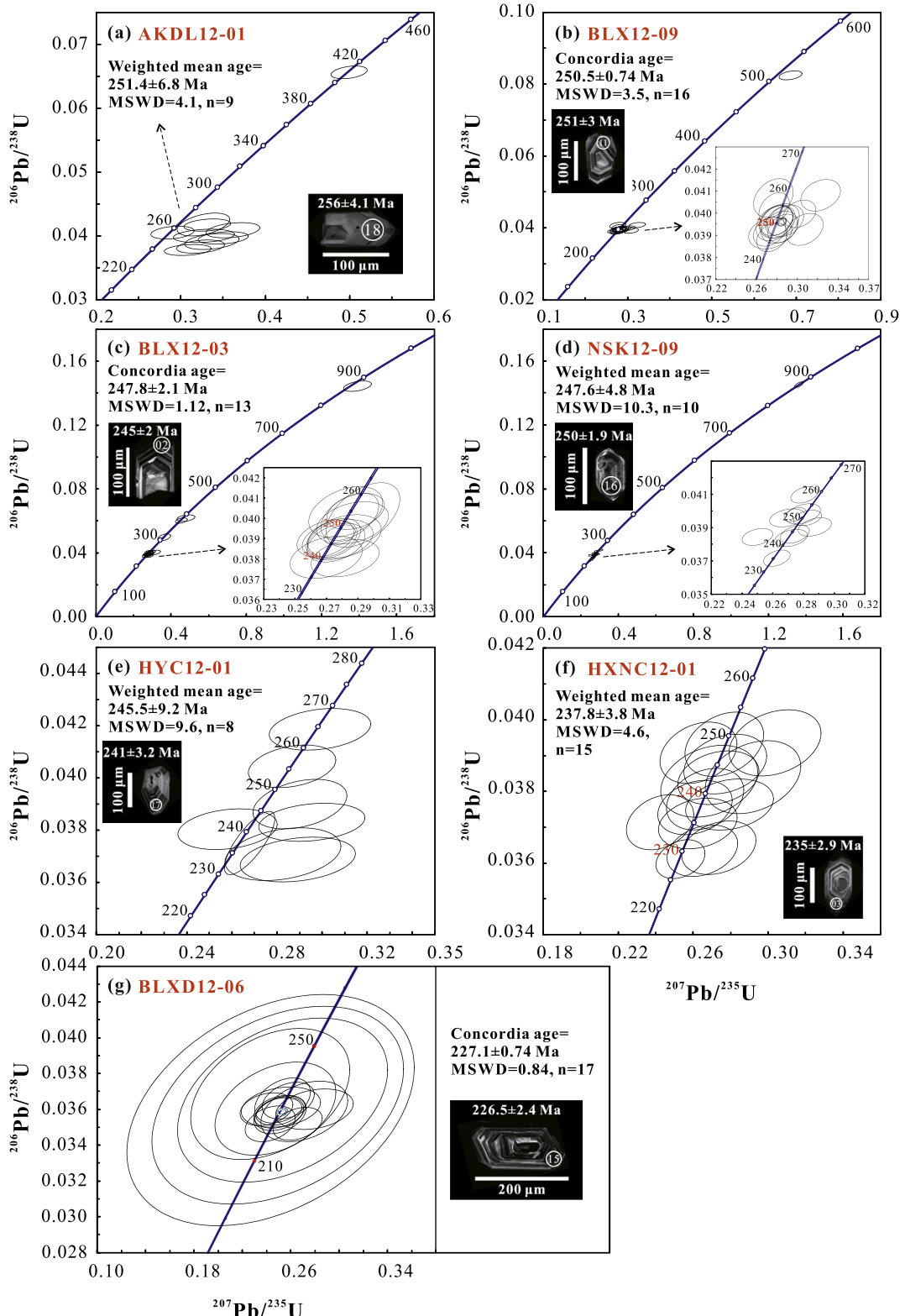


Fig. 3. Concordia diagrams of zircon U–Pb age data and cathodoluminescence images of representative zircons for (a) AKDL12-01, (b) BLX12-09, (c) BLX12-03, (d) NSK12-09, (e) HYC12-01, (f) HXNC12-01 and (g) BLXD12-06 from the Triassic granitoids in the East Kunlun Orogenic Belt. Various amounts of inherited/captured old zircons of ~900 Ma and ~500–300 Ma in the early Triassic granitoids may indicate the presence and involvement of old crustal materials.

Nb, Er, Th, and U, and 10–15% for Ta, Tm and Gd. Full sample preparation techniques and other details are described by Song et al. (2010). Results are listed in Table 2.

3.3. Sr-Nd-Hf isotopes

The whole-rock Sr-Nd-Hf isotopic composition of twenty-two samples were determined at GPMR. Sr and Nd isotopic ratios were

Table 2

Whole-rock major and trace element data of the Triassic granitoids in the East Kunlun Orogenic Belt.

Sample	AKDL12-01	AKDL12-03	AKDL12-04	BLX12-09	BLX12-03	BLX12-06	BLX12-08	HXNC12-07	NSK12-09
Age (Ma)	(Early Triassic)	-251			-248				
<i>Major elements (wt%)</i>									
SiO ₂	72.50	72.24	75.83	63.01	73.19	72.55	72.13	75.40	72.74
TiO ₂	0.44	0.41	0.10	0.65	0.13	0.13	0.13	0.11	0.14
Al ₂ O ₃	13.60	14.17	13.18	16.27	13.96	14.20	14.45	13.84	13.85
Fe ₂ O ₃ ^T	2.87	2.89	0.67	5.67	2.16	1.98	2.09	1.06	2.01
MnO	0.06	0.09	0.02	0.11	0.07	0.04	0.07	0.02	0.06
MgO	0.78	1.09	0.07	1.99	0.22	0.23	0.25	0.16	0.24
CaO	2.73	3.08	0.81	4.90	1.31	1.63	1.40	1.14	1.65
Na ₂ O	3.74	4.97	4.00	3.23	4.12	3.93	4.20	3.30	3.58
K ₂ O	2.37	0.47	4.26	3.05	3.60	3.69	3.86	4.47	4.28
P ₂ O ₅	0.09	0.08		0.17	0.04	0.06		0.03	0.04
LOI	0.71	0.99	0.44	0.49	0.52	0.67	0.53	0.52	0.54
Total	99.89	100.49	99.38	99.52	99.32	99.12	99.12	100.04	99.11
A/NK	17.09	14.07	76.26	7.33	40.97	33.73	37.25	50.11	33.42
A/CNK	0.99	0.99	1.04	0.93	1.07	1.06	1.06	1.12	1.02
Mg [#]	0.37	0.45	0.19	0.44	0.18	0.21	0.21	0.25	0.21
<i>Trace elements (ppm)</i>									
Li	4.47	9.60	2.64	21.8	40.6	14.8	39.9	33.9	50.0
Sc	7.90	7.34	1.95	13.8	3.46	2.88	3.40	3.59	2.28
V	54.6	44.4	2.07	119	4.49	4.66	4.96	3.67	4.88
Cr	4.44	3.78	17.2	10.0	4.82	21.6	4.75	3.00	3.85
Co	5.81	3.39	0.29	11.5	0.93	0.94	0.99	0.53	1.14
Ni	2.51	2.49	8.88	11.8	0.97	8.42	1.63	1.27	0.50
Cu	2.51	0.75	0.24	3.68		2.37		0.08	1.56
Zn	33.5	28.6	6.97	59.1	33.4	21.7	27.6	19.1	27.6
Ga	16.2	15.5	13.9	17.8	17.3	15.8	16.6	21.3	14.6
Rb	65.5	7.73	231	102	157	150	139	200	156
Sr	249	389	48.5	455	113	152	128	198	101
Y	19.0	21.1	15.0	22.5	29.8	21.1	25.7	19.6	18.3
Zr	206	187	56.3	189	119	101	131	96.5	105
Nb	6.94	7.95	14.2	9.77	11.9	9.81	11.4	16.3	10.0
Cs	0.52	0.86	2.60	2.22	3.31	2.72	3.06	4.41	3.42
Ba	734	268	168	845	974	995	1131	1098	447
La	28.0	25.6	22.2	31.8	35.7	37.5	35.6	40.7	19.2
Ce	55.2	51.5	42.2	64.7	68.8	69.7	67.8	80.5	35.4
Pr	5.89	5.57	4.20	7.29	7.34	7.17	7.16	8.85	3.63
Nd	21.3	20.2	13.6	28.0	25.8	24.6	25.0	32.7	12.4
Sm	3.81	3.81	2.53	5.35	4.96	4.34	4.61	6.43	2.55
Eu	1.07	0.85	0.26	1.37	0.73	0.76	0.82	0.96	0.53
Gd	3.53	3.60	2.28	4.85	4.73	3.91	4.36	5.45	2.59
Tb	0.51	0.54	0.34	0.68	0.76	0.57	0.67	0.72	0.43
Dy	3.13	3.43	2.08	4.01	4.76	3.49	4.16	3.81	2.75
Ho	0.66	0.74	0.45	0.81	1.00	0.71	0.87	0.65	0.58
Er	2.12	2.32	1.48	2.45	3.12	2.18	2.69	1.71	1.80
Tm	0.31	0.35	0.23	0.34	0.46	0.32	0.40	0.22	0.28
Yb	2.18	2.40	1.72	2.25	3.18	2.21	2.70	1.30	1.97
Lu	0.34	0.37	0.28	0.33	0.48	0.33	0.41	0.17	0.30
Hf	4.82	4.48	1.88	4.33	3.43	2.79	3.54	3.26	2.96
Ta	0.52	0.52	0.85	0.67	0.75	0.79	0.74	1.11	0.86
Pb	9.12	7.08	15.7	13.6	20.9	14.5	19.1	36.5	22.9
Th	7.45	8.34	25.4	10.0	14.7	16.3	13.9	8.36	13.2
U	1.26	1.38	1.29	1.34	1.72	1.35	1.59	1.59	2.22
(La/Yb) _N	9.22	7.65	9.25	10.13	8.05	12.20	9.46	22.44	6.98
Eu/Eu [*]	0.89	0.70	0.33	0.82	0.46	0.57	0.56	0.50	0.63
Sr/Sr*	0.65	1.06	0.19	0.92	0.24	0.33	0.28	0.34	0.44
Sample	GYK12-05	DGLX12-01	DGL12-01	DGL12-02	HYC12-01	HYC12-06 (host)	WLG12-05	WLG12-07	HXNC12-01
Age (Ma)	(Middle Triassic)	-247			-246		-244		-238
<i>Major elements (wt%)</i>									
SiO ₂	70.68	69.16	67.32	69.08	71.35	68.42	71.12	72.95	68.01
TiO ₂	0.31	0.37	0.57	0.61	0.19	0.39	0.25	0.22	0.43
Al ₂ O ₃	14.83	14.63	16.33	13.83	14.96	15.93	14.20	13.19	15.87
Fe ₂ O ₃ ^T	2.79	3.35	3.60	4.11	1.95	3.13	2.37	1.76	3.02
MnO	0.06	0.07	0.05	0.06	0.06	0.06	0.09	0.02	0.06
MgO	0.62	1.41	1.70	1.19	0.44	1.04	0.58	0.28	0.87
CaO	2.72	3.67	4.11	2.50	2.52	4.21	1.77	0.96	3.27
Na ₂ O	3.55	3.24	3.29	2.66	4.21	4.05	3.28	3.55	3.76
K ₂ O	3.16	2.72	1.43	4.23	2.72	1.18	4.37	4.94	3.40
P ₂ O ₅	0.05	0.07	0.12	0.15	0.07	0.13	0.05	0.02	0.15
LOI	0.49	0.61	0.88	1.12	0.51	0.51	1.54	1.48	0.48
Total	99.25	99.30	99.40	99.53	98.97	99.06	99.64	99.37	99.33
A/NK	17.83	10.97	9.28	14.82	20.59	10.91	24.67	48.54	13.68
A/CNK	1.04	0.98	1.13	1.02	1.03	1.02	1.06	1.02	1.00
Mg [#]	0.33	0.48	0.51	0.39	0.33	0.42	0.35	0.26	0.39

Table 2 (continued)

Sample	GYK12-05	DGLX12-01	DGL12-01	DGL12-02	HYC12-01	HYC12-06 (host)	WLG12-05	WLG12-07	HXNC12-01
Age (Ma)	(Middle Triassic)	~247			-246		-244		~238
<i>Trace elements (ppm)</i>									
Li	65.0	41.2	52.2	57.9	38.4	16.9	15.0	18.7	33.2
Sc	3.70	5.97	10.0	9.92	2.09	2.89	4.92	3.00	3.67
V	10.5	46.8	60.8	35.4	10.9	22.0	20.8	7.99	27.9
Cr	2.75	10.1	31.1	11.1	4.06	5.31	5.74	5.15	3.97
Co	2.04	6.36	5.90	6.43	1.57	3.28	2.03	1.13	3.39
Ni	0.70	5.07	8.68	2.78	0.90	2.17	2.72	1.45	1.62
Cu	0.37	1.33	1.38	4.75		0.16	3.61	0.44	0.54
Zn	58.1	50.5	50.0	80.5	53.2	56.8	50.3	43.5	48.4
Ga	19.6	16.5	20.3	21.9	20.0	16.9	16.8	20.6	19.0
Rb	117	105	102	260	76.0	38.4	149	257	131
Sr	297	397	311	134	406	569	257	57.1	458
Y	13.5	10.8	13.3	24.4	6.27	3.91	12.0	43.7	8.60
Zr	153	107	184	281	92.1	111	167	227	197
Nb	13.1	7.56	7.13	13.0	10.4	5.45	12.9	14.4	9.50
Cs	3.96	3.18	10.3	10.1	2.55	0.72	2.99	5.04	1.91
Ba	471	697	240	546	852	420	1298	282	818
La	20.0	21.4	20.6	47.9	27.6	22.1	40.6	46.2	28.5
Ce	39.2	39.4	43.6	104	51.4	41.8	70.8	102	51.7
Pr	4.34	4.19	5.00	11.6	5.16	4.47	6.89	11.1	5.49
Nd	15.7	15.0	19.4	43.2	17.1	15.5	23.0	41.5	19.4
Sm	3.15	2.70	3.83	7.76	2.47	2.14	3.84	8.64	3.20
Eu	0.65	0.81	1.03	1.09	0.78	0.86	0.84	0.40	0.86
Gd	2.84	2.39	3.43	6.28	1.83	1.50	3.25	8.15	2.46
Tb	0.43	0.32	0.47	0.81	0.22	0.16	0.42	1.22	0.30
Dy	2.46	1.86	2.59	4.37	1.10	0.74	2.25	7.39	1.55
Ho	0.47	0.38	0.50	0.85	0.20	0.13	0.43	1.52	0.29
Er	1.32	1.12	1.41	2.49	0.57	0.37	1.20	4.57	0.83
Tm	0.19	0.16	0.20	0.35	0.08	0.05	0.16	0.65	0.11
Yb	1.23	1.09	1.28	2.29	0.51	0.32	1.02	4.27	0.79
Lu	0.17	0.17	0.19	0.35	0.08	0.05	0.16	0.62	0.12
Hf	3.86	2.70	4.24	6.40	2.70	2.74	4.01	6.32	4.59
Ta	0.80	0.50	0.44	0.88	0.70	0.38	0.79	0.92	0.64
Pb	19.2	14.6	13.3	26.9	16.2	7.41	28.2	22.8	18.6
Th	6.64	9.42	5.71	24.3	4.89	3.83	17.7	21.9	8.04
U	1.04	1.75	1.25	3.96	0.69	0.43	1.45	4.33	0.99
(La/Yb) _N	11.67	14.14	11.49	15.00	38.72	49.23	28.46	7.77	25.83
Eu/Eu [*]	0.67	0.98	0.87	0.48	1.12	1.47	0.73	0.15	0.94
Sr/Sr [*]	1.04	1.45	0.91	0.17	1.25	1.98	0.59	0.08	1.28
Sample	HXNC12-05	ZJX12-01		WLS12-01	BLX12-15 (host)		DGL12-05	DGL12-07	BLXD12-02
Age (Ma)	~238	(Late Triassic)	~234	~227	~222		~215		~214
<i>Major elements (wt%)</i>									
SiO ₂	60.06	63.86		74.78	64.10		74.75	73.38	72.82
TiO ₂	0.95	0.68		0.10	0.66		0.17	0.21	0.24
Al ₂ O ₃	16.06	16.81		12.94	15.72		12.72	13.32	13.29
Fe ₂ O ₃ ^T	7.29	4.33		1.47	4.50		1.60	1.90	2.44
MnO	0.10	0.07		0.04	0.07		0.01	0.03	0.04
MgO	2.96	1.88		0.12	2.05		0.21	0.15	0.48
CaO	6.02	4.40		0.94	4.27		0.76	0.85	1.66
Na ₂ O	3.26	3.65		3.58	3.59		3.34	3.62	3.54
K ₂ O	1.94	3.16		4.47	2.59		5.02	5.55	3.65
P ₂ O ₅	0.24	0.17		0.03	0.18		0.02	0.05	0.14
LOI	1.60	0.84		0.76	1.27		0.70	0.56	1.08
Total	100.48	99.86		99.24	99.01		99.31	99.61	99.39
A/NK	5.27	8.11		61.55	8.00		63.95	62.73	28.13
A/CNK	0.87	0.96		1.04	0.95		1.03	0.98	1.04
Mg [#]	0.47	0.49		0.15	0.50		0.22	0.15	0.30
<i>Trace elements (ppm)</i>									
Li	49.0	48.4		10.7	15.9		15.9	21.3	24.5
Sc	18.3	8.15		2.11	10.3		2.18	2.83	3.83
V	153	60.4		2.19	100		3.15	6.55	19.5
Cr	17.9	14.7		18.4	17.5		2.65	10.3	8.11
Co	15.4	7.04		0.64	10.9		0.55	0.89	2.59
Ni	5.91	5.05		8.16	6.52		0.48	5.47	4.69
Cu	6.08	1.61		2.03	1.66		0.59	0.17	2.37
Zn	68.1	58.9		23.3	49.6		42.1	45.6	44.6
Ga	20.8	19.7		17.4	20.3		20.7	22.5	16.9
Rb	87.7	132		158	94.1		244	205	157
Sr	387	422		153	497		28.4	39.9	153
Y	18.8	15.4		10.8	14.4		49.5	33.1	31.4
Zr	136	196		102	159		208	272	136
Nb	11.3	10.2		11.7	11.9		13.4	12.4	28.5

(continued on next page)

Table 2 (continued)

Sample	HXNC12-05	ZJX12-01	WLS12-01	BLX12-15 (host)	DGL12-05	DGL12-07	BLXD12-02
Age (Ma)	~238	(Late Triassic) ~234	~227	~222	~215		~214
Cs	2.40	10.8	2.51	3.71	7.24	6.04	4.66
Ba	357	534	2012	684	173	235	507
La	37.9	24.2	48.3	31.9	61.6	89.7	29.4
Ce	72.9	49.4	89.8	63.5	129	186	63.8
Pr	8.04	5.73	8.85	6.83	14.0	19.1	7.39
Nd	31.4	21.4	29.2	24.5	50.1	68.0	27.3
Sm	5.88	4.16	4.24	4.28	10.1	11.4	5.76
Eu	1.22	1.06	0.94	1.09	0.30	0.41	0.65
Gd	5.37	3.54	3.18	3.63	9.29	9.38	5.28
Tb	0.71	0.48	0.38	0.48	1.40	1.21	0.82
Dy	3.89	2.68	1.94	2.63	8.53	6.64	5.12
Ho	0.74	0.51	0.36	0.50	1.69	1.28	1.06
Er	2.02	1.44	1.08	1.43	4.89	3.67	3.28
Tm	0.25	0.19	0.15	0.20	0.66	0.48	0.49
Yb	1.52	1.30	1.03	1.29	4.36	3.07	3.31
Lu	0.22	0.18	0.16	0.19	0.61	0.44	0.48
Hf	3.23	4.68	2.48	3.90	6.38	6.96	3.73
Ta	0.81	0.60	0.69	0.78	0.84	0.88	1.86
Pb	10.8	18.7	23.3	10.7	26.4	25.2	20.9
Th	5.23	8.00	14.7	11.2	22.5	17.4	22.5
U	0.80	1.46	2.23	1.79	2.97	1.96	2.61
(La/Yb) _N	17.84	13.41	33.59	17.77	10.12	20.94	6.37
Eu/Eu*	0.67	0.84	0.78	0.85	0.09	0.12	0.36
Sr/Sr*	0.71	1.11	0.28	1.11	0.03	0.03	0.31

A/NK = molar $\text{Al}_2\text{O}_3/(\text{Na}_2\text{O} + \text{K}_2\text{O})$, A/CNK = molar $\text{Al}_2\text{O}_3/(\text{CaO} + \text{Na}_2\text{O} + \text{K}_2\text{O})$, Mg# = molar $\text{Mg}^{2+}/(\text{Mg}^{2+} + \text{Fe}^{2+})$; LOI, loss on ignition. $(\text{La/Yb})_N$ refers to the value normalized against chondrite. Eu/Eu* = $\text{Eu}_{\text{PM}}/[\text{Sm}_{\text{PM}} \times \text{Gd}_{\text{PM}}]^{1/2}$, Sr/Sr* = $\text{Sr}_{\text{PM}}/[\text{Pr}_{\text{PM}} \times \text{Nd}_{\text{PM}}]^{1/2}$, where subscript PM denotes normalized values against primary mantle.

measured on a Thermo Finnigan Triton Ti thermal ionization mass spectrometer (TIMS). Analytical details are given in Gao et al. (2004). And Hf isotopic analysis was conducted using a multi-collector inductively coupled plasma mass spectrometer (MC-ICP-MS) with a Thermo Neptune Plus system. The procedures of chemical separation and analysis are following Yang et al. (2010b). The isotopic data are presented in Table 3.

4. Results

4.1. Zircon U—Pb ages

Zircons from all the analytical samples are transparent, light brown euhedral columnar crystals. They have faint (Fig. 3a), oscillatory (Fig. 3b, c, f, g), sector (Fig. 3e) and transitional (Fig. 3d) zoning, which is consistent with a magmatic origin (Corfu et al., 2003). The LA-ICP-MS U—Pb analysis gave variable Th (101–4815 ppm) and U (115–8483 ppm) concentrations with Th/U ratios of 0.15–1.21, which are of a magmatic origin (Hoskin and Schaltegger, 2003). Thus, the youngest U—Pb age group of the zircons represents the crystallization age. All the data are given in Appendix A.

Zircons from sample AKDL12-01 and NSK12-09 yield weighted mean $^{206}\text{Pb}/^{238}\text{U}$ ages of 251.4 ± 6.8 Ma (MSWD = 4.1, n = 9) and 247.6 ± 4.8 Ma (MSWD = 10.3, n = 10), respectively. And zircons from sample BLX12-09 and BLX12-03 yield concordia ages of 250.5 ± 0.74 Ma (MSWD = 3.5, n = 16) and 247.8 ± 2.1 Ma (MSWD = 1.12, n = 13), respectively. Inherited /Captured zircon cores plotted along the concordia yield age group of ~900 Ma and ~500–300 Ma (Figs. 3a-d), closing to the age of crust basement of the EKOB (Xiaomiao Formation) and later metamorphism as well as anatexis event (Wang et al., 2004). Zircons from sample HYC12-01 and HXNC12-01 yield weighted mean $^{206}\text{Pb}/^{238}\text{U}$ ages of 245.5 ± 9.2 Ma (MSWD = 9.6, n = 8) and 237.8 ± 3.8 Ma (MSWD = 4.6, n = 15), and the concordia age 227.1 ± 0.74 Ma (MSWD = 0.84, n = 17) is given by zircons from sample BLXD12-06, respectively. Our new data can be considered as approximating the emplacement ages of the granitoids in the EKOB,

which, together with the high-quality zircon U—Pb ages reported in the recent literature (summarized in Table 1), indicate that these granitoids continually formed from early Triassic (~251 Ma) to late Triassic (~214 Ma).

4.2. Major and trace elements

The Triassic granitoids from the EKOB show high SiO_2 (60.06–75.83 wt%) and low $\text{Na}_2\text{O} + \text{K}_2\text{O}$ (4.72–9.17 wt%) with a relatively narrow compositional range from diorite, granodiorite to granite in total alkali ($\text{Na}_2\text{O} + \text{K}_2\text{O}$)- SiO_2 space (Fig. 4a). In the ($\text{Na}_2\text{O} + \text{K}_2\text{O}$ -CaO) against SiO_2 discrimination diagram (Fig. 4b), most of these rocks are restricted in the calc-alkaline field with scattered ones falling in the alkali-calcic and calcic fields. The early Triassic granitoids varying from low-K calc-alkaline series to high-K calc-alkaline series ($\text{K}_2\text{O} = 0.47$ –4.47 wt%). Comparatively, the middle Triassic granitoids fall in the calc-alkaline and high-K calc-alkaline fields ($\text{K}_2\text{O} = 1.18$ –4.94 wt%). The late Triassic granitoids with higher K_2O of 2.59–5.55 wt% belong to high-K calc-alkaline and shoshonite series (Fig. 4c). They are all weakly metaluminous to peraluminous ($\text{A/NK} = 1.11$ –2.34, $\text{A/CNK} = 0.87$ –1.13), which are equivalent to I-type granitoids with only two samples straddling the I- to S-type boundary (Fig. 4d). As expected, these Triassic granitoids display decreasing trends in major elements with increasing SiO_2 (Fig. 5).

The Triassic granitoids invariably show enrichment of light rare earth elements (LREE) with $(\text{La/Yb})_N$ of 6.37–49.23. Most samples show significant negative Eu anomalies with a few showing weak positive Eu anomalies ($\text{Eu/Eu}^* = 0.09$ –1.47; Table 2 and Figs. 6a-c). They share similar primitive mantle normalized patterns with enrichment in Rb (although one sample of the early Triassic granitoids is distinct), K, Pb and depletion in Nb, Ta, P, Ti, resembling the composition of the bulk continental crust (BCC; Rudnick and Gao, 2003), as well as variable Sr anomalies (Sr/Sr* of 0.19–1.06 for T₁ granitoids, 0.08–1.98 for T₂ granitoids and 0.03–1.11 for T₃ granitoids) (Table 2).

Table 3

Whole rock Sr-Nd-Hf isotopic composition of the Triassic granitoids from the East Kunlun Orogenic Belt.

Sample	Rb	Sr	$^{87}\text{Rb}/^{86}\text{Sr}$	$^{87}\text{Sr}/^{86}\text{Sr}$	$\pm 2\sigma$	I_{sr}	Sm	Nd	$^{147}\text{Sm}/^{144}\text{Nd}$	$^{143}\text{Nd}/^{144}\text{Nd}$	$\pm 2\sigma$	$^{143}\text{Nd}/^{144}\text{Nd}_{\text{di}}$	$\varepsilon_{\text{Nd}}(t)$	Lu	Hf	$^{176}\text{Lu}/^{177}\text{Hf}$	$^{176}\text{Hf}/^{177}\text{Hf}$	$\pm 2\sigma$	$^{176}\text{Hf}/^{177}\text{Hf}$	$\varepsilon_{\text{Hf}}(t)$	t (Ma)
<i>T₁ group</i>																					
BLX12-09	102	455	0.65	0.710934	6	0.708626	5.35	28.0	0.12	0.512222	3	0.512030	-5.55	0.33	4.33	0.01	0.282553	2	0.282501	-4.06	251
AKDL12-01	65.5	249	0.76	0.709400	5	0.706684	3.81	21.3	0.11	0.512409	4	0.512230	-1.66	0.34	4.82	0.01	0.282765	2	0.282718	3.59	251
AKDL12-03	7.73	389	0.06	0.707823	3	0.707617	3.81	20.2	0.11	0.512405	6	0.512216	-1.92	0.37	4.48	0.01	0.282762	2	0.282707	3.21	251
HXNC12-07	200	198	2.92	0.725152	5	0.714843	6.43	32.7	0.12	0.512138	5	0.511944	-7.32	0.17	3.26	0.01	0.282509	3	0.282474	-5.11	248
NSK12-09	156	101	4.46	0.726310	6	0.710573	2.55	12.4	0.12	0.512272	4	0.512069	-4.88	0.30	2.96	0.01	0.282636	3	0.282569	-1.74	248
BLX12-03	157	113	4.01	0.725105	5	0.710972	4.96	25.8	0.12	0.512171	3	0.511981	-6.59	0.48	3.43	0.02	0.282588	3	0.282496	-4.31	248
BLX12-06	150	152	2.87	0.721635	3	0.711511	4.34	24.6	0.11	0.512153	3	0.511979	-6.64	0.33	2.79	0.02	0.282577	3	0.282499	-4.20	248
BLX12-08	139	128	3.13	0.721689	5	0.710650	4.61	25.0	0.11	0.512167	3	0.511985	-6.52	0.41	3.54	0.02	0.282584	3	0.282508	-3.88	248
AKDL12-04	231	48.5	13.80	0.755502	5	0.706213	2.53	13.6	0.11	0.512332	4	0.512146	-3.30	0.28	1.88	0.02	0.282713	4	0.282615	-0.05	251
<i>T₂ group</i>																					
GYK12-05	117	297	1.15	0.718030	4	0.714006	3.15	15.7	0.12	0.512161	5	0.511963	-6.97	0.17	3.86	0.01	0.282512	2	0.282483	-4.81	247
DGLX12-01	105	397	0.77	0.711228	5	0.708529	2.70	15.0	0.11	0.512304	4	0.512127	-3.76	0.17	2.70	0.01	0.282633	3	0.282592	-0.93	247
DGL12-02	260	134	5.60	0.752345	4	0.732679	7.76	43.2	0.11	0.512025	3	0.511848	-9.21	0.35	6.40	0.01	0.282443	3	0.282407	-7.50	247
HYC12-06 (host)	38.4	569	0.20	0.712135	5	0.711452	2.14	15.5	0.08	0.512157	4	0.512022	-5.85	0.05	2.74	0.00	0.282532	3	0.282520	-3.51	246
WLG12-05	149	257	1.68	0.713781	3	0.707954	3.84	23.0	0.10	0.512294	3	0.512131	-3.76	0.16	4.01	0.01	0.282619	3	0.282594	-0.96	244
HXNC12-01	131	458	0.83	0.712664	5	0.709853	3.20	19.4	0.10	0.512214	3	0.512058	-5.35	0.12	4.59	0.00	0.282558	2	0.282541	-2.94	238
HXNC12-05	87.7	387	0.66	0.712885	4	0.710665	5.88	31.4	0.11	0.512205	4	0.512027	-5.94	0.22	3.23	0.01	0.282554	3	0.282511	-4.01	238
<i>T₃ group</i>																					
ZJX12-01	132	422	0.91	0.712378	4	0.709362	4.16	21.4	0.12	0.512172	4	0.511990	-6.76	0.18	4.68	0.01	0.282481	3	0.282456	-6.04	234
WLS12-01	158	153	2.99	0.718922	4	0.709265	4.24	29.2	0.09	0.512239	5	0.512108	-4.65	0.16	2.48	0.01	0.282575	3	0.282536	-3.36	227
BLX12-15 (host)	94.1	497	0.55	0.710661	5	0.708930	4.28	24.5	0.11	0.512213	3	0.512059	-5.73	0.19	3.90	0.01	0.282557	2	0.282529	-3.74	222
DGL12-05	244	28.4	24.95	0.855875	5	0.779601	10.1	50.1	0.12	0.512224	3	0.512051	-6.05	0.61	6.38	0.01	0.282655	3	0.282601	-1.34	215
DGL12-07	205	39.9	14.90	0.800046	4	0.754482	11.4	68.0	0.10	0.512180	4	0.512036	-6.34	0.44	6.96	0.01	0.282604	3	0.282567	-2.53	215
BLXD12-02	157	153	2.97	0.719073	4	0.710046	5.76	27.3	0.13	0.512221	4	0.512041	-6.27	0.48	3.73	0.02	0.282586	3	0.282512	-4.49	214

$$I_{\text{sr}} = [(^{87}\text{Sr}/^{86}\text{Sr}) - (^{87}\text{Rb}/^{86}\text{Sr})(e^{\lambda t} - 1)]; ^{143}\text{Nd}/^{144}\text{Nd}_{\text{di}} = [(^{143}\text{Nd}/^{144}\text{Nd}) - (^{147}\text{Sm}/^{144}\text{Nd})(e^{N_L} - 1)]; \varepsilon_{\text{Nd}}(t) = [(^{143}\text{Nd}/^{144}\text{Nd}_{\text{di}})/(^{143}\text{Nd}/^{144}\text{Nd}_{\text{CHUR}}) - 1] \times 10^4; ^{176}\text{Hf}/^{177}\text{Hf}_i = [(^{176}\text{Hf}/^{177}\text{Hf}) - (^{176}\text{Lu}/^{177}\text{Hf})(e^{N_L} - 1)]; \varepsilon_{\text{Hf}}(t) = [(^{176}\text{Hf}/^{177}\text{Hf}_i)/(^{176}\text{Hf}/^{177}\text{Hf}_{\text{CHUR}}) - 1] \times 10^4. ^{147}\text{Sm}/^{144}\text{Nd}_{\text{CHUR}} = 0.1967; ^{143}\text{Nd}/^{144}\text{Nd}_{\text{CHUR}} = 0.512638; ^{176}\text{Lu}/^{177}\text{Hf}_{\text{CHUR}} = 0.0332; ^{176}\text{Hf}/^{177}\text{Hf}_{\text{CHUR}} = 0.282772; \lambda(^{87}\text{Rb}) = 1.42 \times 10^{-11} \text{ yr}^{-1}; \lambda(^{147}\text{Sm}) = 6.54 \times 10^{-12} \text{ yr}^{-1}, \lambda(^{176}\text{Lu}) = 1.865 \times 10^{-11} \text{ yr}^{-1}.$$

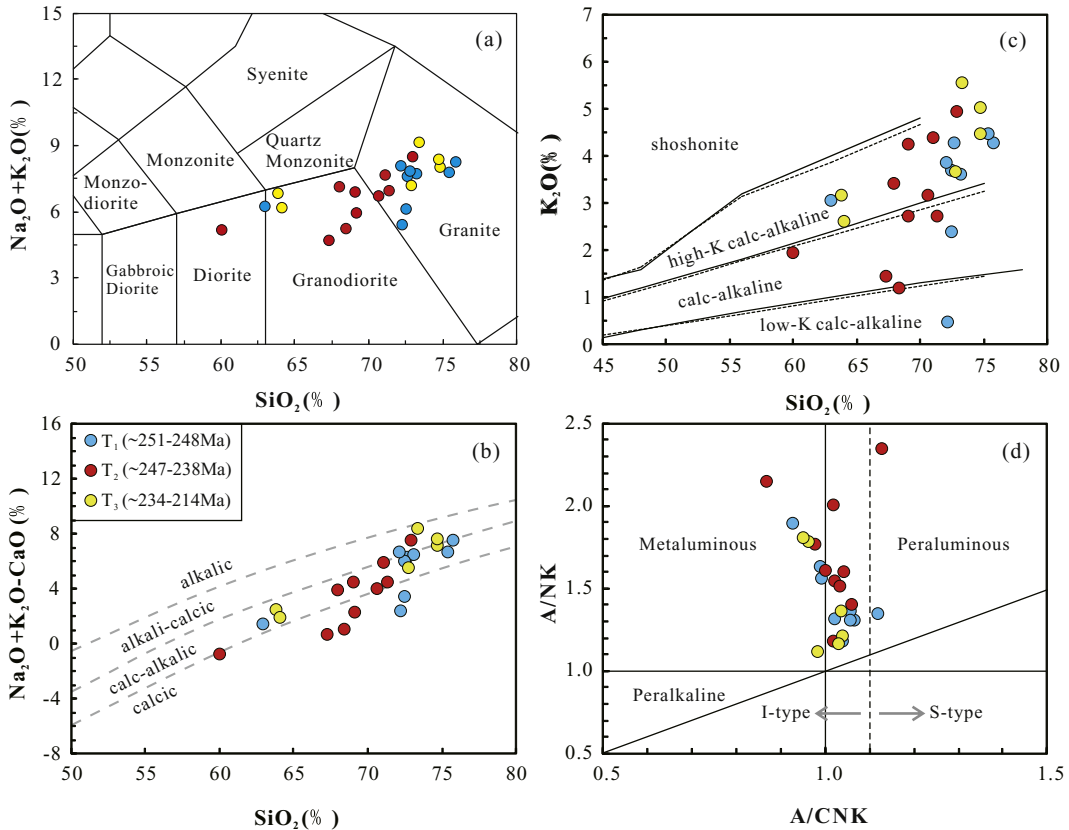


Fig. 4. Plots of (a) $\text{Na}_2\text{O} + \text{K}_2\text{O}$ against SiO_2 (Middlemost, 1994); (b) $\text{Na}_2\text{O} + \text{K}_2\text{O}-\text{CaO}$ against SiO_2 (Frost et al., 2001); (c) K_2O against SiO_2 (Rickwood, 1989); (d) A/NK (molar $\text{Al}_2\text{O}_3/[\text{Na}_2\text{O} + \text{K}_2\text{O}]$) against A/CNK (molar $\text{Al}_2\text{O}_3/[\text{CaO} + \text{Na}_2\text{O} + \text{K}_2\text{O}]$) (Chappell and White, 2001; Maniar and Piccoli, 1989) for the Triassic granitoids from the East Kunlun Orogenic Belt.

4.3. Sr-Nd-Hf isotopes

Bulk-rock Sr-Nd-Hf isotopic data (Table 3) are plotted in Figs. 7–10. Three samples (AKDL12-04, DGL12-05 and DGL12-07) give very high $^{87}\text{Sr}/^{86}\text{Sr}$ (0.7555–0.8559) because of the high Rb/Sr (13.8–24.9) (Table 3), due to significant plagioclase-dominated (and alkali feldspars to some content) fractional crystallization, resembling peralkaline rhyolites (Shao et al., 2015). Such high Rb/Sr resulting in high radiogenic ^{87}Sr ingrowth, which makes the calculated $I_{\text{Sr}}(t)$ unreliable (Wu et al., 2000). Eliminating these samples with inaccurate I_{Sr} (not shown in the Figs. 7–10), the Triassic granitoids have variable I_{Sr} of 0.7067–0.7327. The $\varepsilon_{\text{Nd}(t)}$ and $\varepsilon_{\text{Hf}(t)}$ of all samples range from −9.21 to −1.66 and −7.50 to 3.59, respectively.

5. Discussion

5.1. FC (fractional crystallization) or AFC (assimilation and fractional crystallization)

The data shown in SiO_2 -variation diagrams (Fig. 5) are to a first-order consistent with varying extent of fractional crystallization of hornblende, plagioclase, Fe–Ti oxides and apatite. However, these trends are also consistent with modal variations of these phases in the samples although the depletion in P, Ti, Sr and Eu emphasizes the significance of fractional crystallization.

Crustal assimilation and fractional crystallization (AFC) of mantle-derived mafic magma generally produce continuous compositions from basaltic to felsic and typical linear trends between SiO_2 and $I_{\text{Sr}}/\varepsilon_{\text{Nd}(t)}$, because of high $^{87}\text{Sr}/^{86}\text{Sr}$ and low $^{143}\text{Nd}/^{144}\text{Nd}$ in the upper continental crust. There is a narrow spectrum of rock composition (Fig. 4a) and lack of linear trends in plots of SiO_2 against I_{Sr} and $\varepsilon_{\text{Nd}(t)}$

(Fig. 7a–b). Additionally, they have lower $\text{K}_2\text{O}/\text{Na}_2\text{O}$ than the melts produced by assimilation experiments simulating the reaction between basalts and felsic pelitic gneiss in the crust (Castro, 2001) (Fig. 7d). These suggest that the AFC from common parental mantle-derived mafic magmas is unlikely an important mechanism for the Triassic granitoids from the EKOB. Alternatively, they show variable REE patterns and a wide range of bulk-rock Sr-Nd-Hf isotopic compositions from the early to late Triassic (Figs. 6a–c and 7a–c), which may indicate different sources and/or different petrogenetic processes. However, any petrogenetic model must satisfy the observation that the Triassic granitoids have hybrid mantle-crust geochemical signatures, as evidenced by their Sr-Nd-Hf isotopic compositions (Figs. 8, 9 and 10).

5.2. Petrogenesis

S-, I-, A- and M-type granites are widely used classifications on the basis and sources and petrogenesis (Chappell and White, 2001; Collins et al., 1982; Whalen et al., 1987). Chemically, the Triassic granitoids from the EKOB have relatively low A/CNK values (≤ 1.1 ; Fig. 4d) and amphiboles and biotite are common (Fig. 2), which accord with features of I-type granites (Chappell and White, 2001). Therefore, the Triassic granitoids from the EKOB are I-type granites, to be exact, they are calc-alkaline I-type granitoids as shown in Fig. 4. Such rocks can form by (1) crustal assimilation and fractional crystallization of mantle-derived mafic magma (AFC) (Chen and Arakawa, 2005; De Souza et al., 2007); (2) partial melting of crustal materials at deep or shallow (Laurent et al., 2014; Liu et al., 2015); (3) hybridization between mantle-derived mafic magmas and crustal melts (Dong et al., 2011); (4) partial melting of remained basaltic ocean crust with sediment mélange (Castro et al., 2010; Huang et al., 2014; Kong et al., 2017; Shao et al., 2017; Zhang et al., 2016).

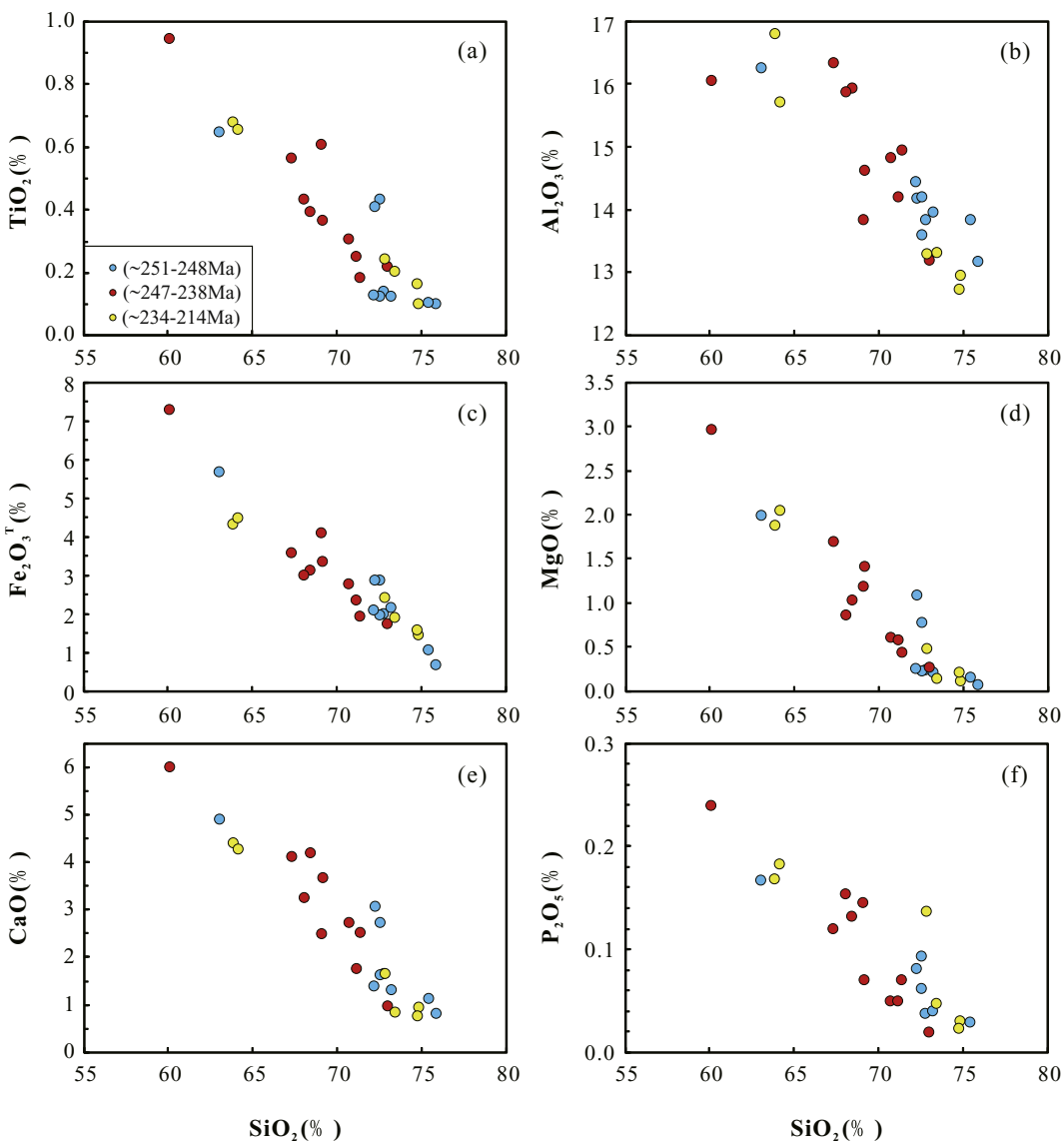


Fig. 5. SiO_2 variation diagrams of the granitoids from the East Kunlun Orogenic Belt.

5.2.1. Petrogenesis of the early Triassic (~251–248 Ma) granitoids

The early Triassic granitoids (T_1 , ~251–248 Ma) are enriched in Rb, K, Pb and depleted in Nb, Ta, Sr, P and Ti, which resembles the composition of the bulk continental crust (BCC; Fig. 6d). Abnormally, the sample (AKDL12-03) displays strong negative Rb anomaly due to its extremely low content of Rb (7.7 ppm). It may be attributed to some possible reasons such as strong alteration. The T_1 granitoids have higher I_{Sr} (0.7067–0.7148), negative $\varepsilon_{\text{Nd(t)}}$ (−7.32 to −1.66) and negative to positive $\varepsilon_{\text{Hf(t)}}$ (−5.11 to 3.59) than the mature continental crust ($^{87}\text{Sr}/^{86}\text{Sr}_i = 0.73802$, $\varepsilon_{\text{Nd(t)}} = -17.0$, $\varepsilon_{\text{Hf(t)}} = -15.5$; Shao et al., 2017), suggesting significant mantle contribution (or juvenile crustal material) in terms of isotopes. The Hf isotopic data of the T_1 granitoids and the other Kunlun Triassic granitoids (Fig. 9; Ding et al., 2015; Huang et al., 2014; Xia et al., 2015; Zhang et al., 2016; Shao et al., 2017) are also indicative of significant mantle contribution. To produce such andesitic to felsic BCC-like magmas with mantle signature, it requires a basaltic source plus continental materials mentioned above. As shown in many previous studies, the A'nyemaqen Ocean (the north branch of the Paleo-Tethys Ocean recorded in the EKOB; Jiang et al., 1992) had closed and recorded a syn-collisional setting in the early Triassic (Huang et al., 2014; Shao et al., 2017), in which setting the

potential basaltic source may be the arc crust (island arc basalt, IAB) or the subducted ocean crust (mid-ocean ridge basalt, MORB). Higher Sr/Sr^* values of IAB (~2.72) than that of BCC (0.933) and MORB (~0.1–2.0) have been used by Niu and co-authors (Niu and O'Hara, 2009; Niu et al. (2013) to argue against IAB for the source of T_1 granitoids ($\text{Sr/Sr}^* = 0.19$ –1.06). Therefore, the basaltic end-member for the source of T_1 granitoids is most probably supplied by the subducted ocean crust (i.e. MORB). Note that their flat HREE (mean $[\text{Dy/Yb}]_N = 1.1$, the same as BCC) patterns and constant $(\text{Ce/Yb})_N$ with decrease Yb_N (Fig. 6a, d), requires melting under amphibolite facies conditions (< 50 km; without garnet signature). Additionally, the trace element patterns, as well as the isotopic composition, especially the Nd–Hf isotopes of the T_1 (~251–248 Ma) granitoids are consistent with the I-type syn-collisional granitoids derived from melting of subducted oceanic crust with terrigenous sediments of upper continental crust origin (Figs. 7a, b, c and 8, 9, 10). Partial melting of the ocean crust produces felsic melts and the ocean crust derived from the mantle not long ago imparts the mantle isotopic signature (Niu et al., 2013). Meanwhile, the addition of terrigenous sediment can explain the crustal signatures of the T_1 granitoids. Many lines of evidence above suggest the T_1 (~251–248 Ma) granitoids are derived from partial melting of

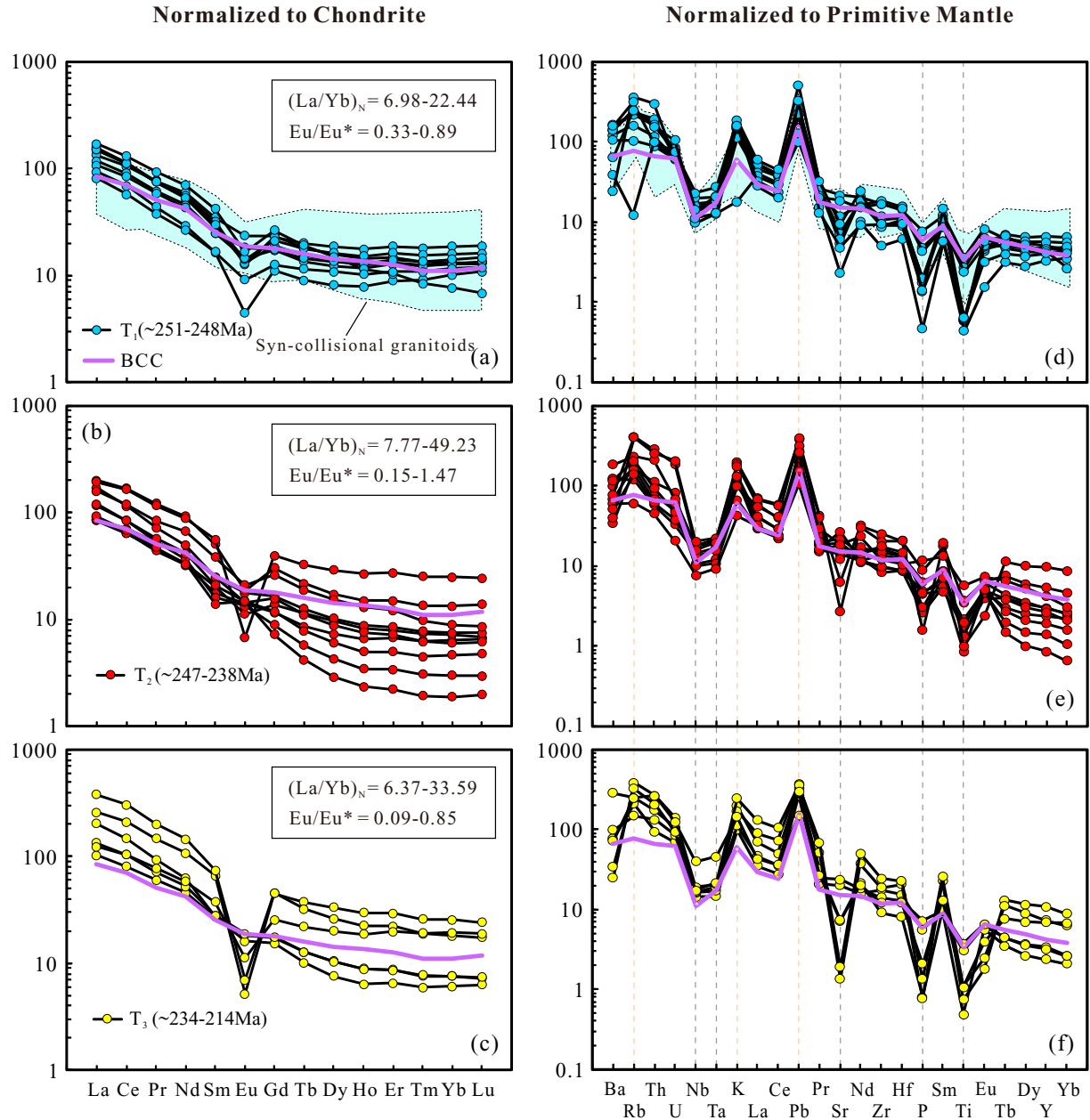


Fig. 6. (a-c) Normalized rare earth element (REE) and (d-f) multi-element patterns of the Triassic granitoids from the East Kunlun Orogenic Belt. Bulk continental crust (BCC; Rudnick and Gao, 2003) composition is also plotted for comparison. Chondrite and primitive mantle data are from Sun and McDonough (1989). The shaded fields in (a) and (d) are of I-type syn-collisional granitoids derived from subducted oceanic crust in the East Kunlun Orogenic Belt (Huang et al., 2014).

remaining fragments of the subducted A'nyemaqen ocean crust with recycled terrigenous sediment under amphibolite facies conditions. The underthrusting cold Anyemaqen Ocean crust evolves along a high T/P geothermal path and has longer time to absorb heat from the prior hot active continental margin. The highly hydrated ocean crust (along with terrigenous sediments) begins to melt when it reaches the hydrous basaltic solidus (<700 °C) under amphibolite conditions (see details in Mo et al., 2008; Niu et al., 2013). The melts subsequently underwent plagioclase-controlled fractionation within crustal reservoirs supported by relatively large decrease in Al₂O₃, CaO (Fig. 5b, e) and Sr, Eu (Fig. 7e, f) with small increase in SiO₂. It should be noted that the initial isotopic ratio (Isr , ε_{Nd} (t) and ε_{Hf} (t)) variations within individual outcrops largely reflect small scale isotopic heterogeneity due to incomplete homogenization of melts affected by crustal assimilation or modal variation or both. This is because granitoid magmas under sub-liquidus conditions

are “crystal mashes”, complete homogenization is thus restricted by the efficient diffusion (Ramos and Reid, 2005). Inherited/captured zircon cores plotted along the concordia yield age group of ~900 Ma and ~500-300 Ma (Figs. 3a-d), closing to the age of crust basement of the EKOB (Xiaomiao Formation) and later metamorphism (Wang et al., 2004), implying that they were involved in the ~250 Ma magmatism. Terrigenous sediments melted alongside oceanic crust also result in the isotope heterogeneity.

Studies of the Linzizong volcanic succession (LVS) in southern Tibet have testified that juvenile continental crust is produced via partial melting of the ocean crust under the amphibolite facies conditions and preserved as ‘net crust growth’ in the collision zones (Mo et al., 2008; Niu et al., 2013; Niu and O'Hara, 2009). The syn-collisional East Kunlun granitoids provide more geochemical and isotopic data to support this hypothesis. Firstly, the bulk compositions of granitoids are similar to

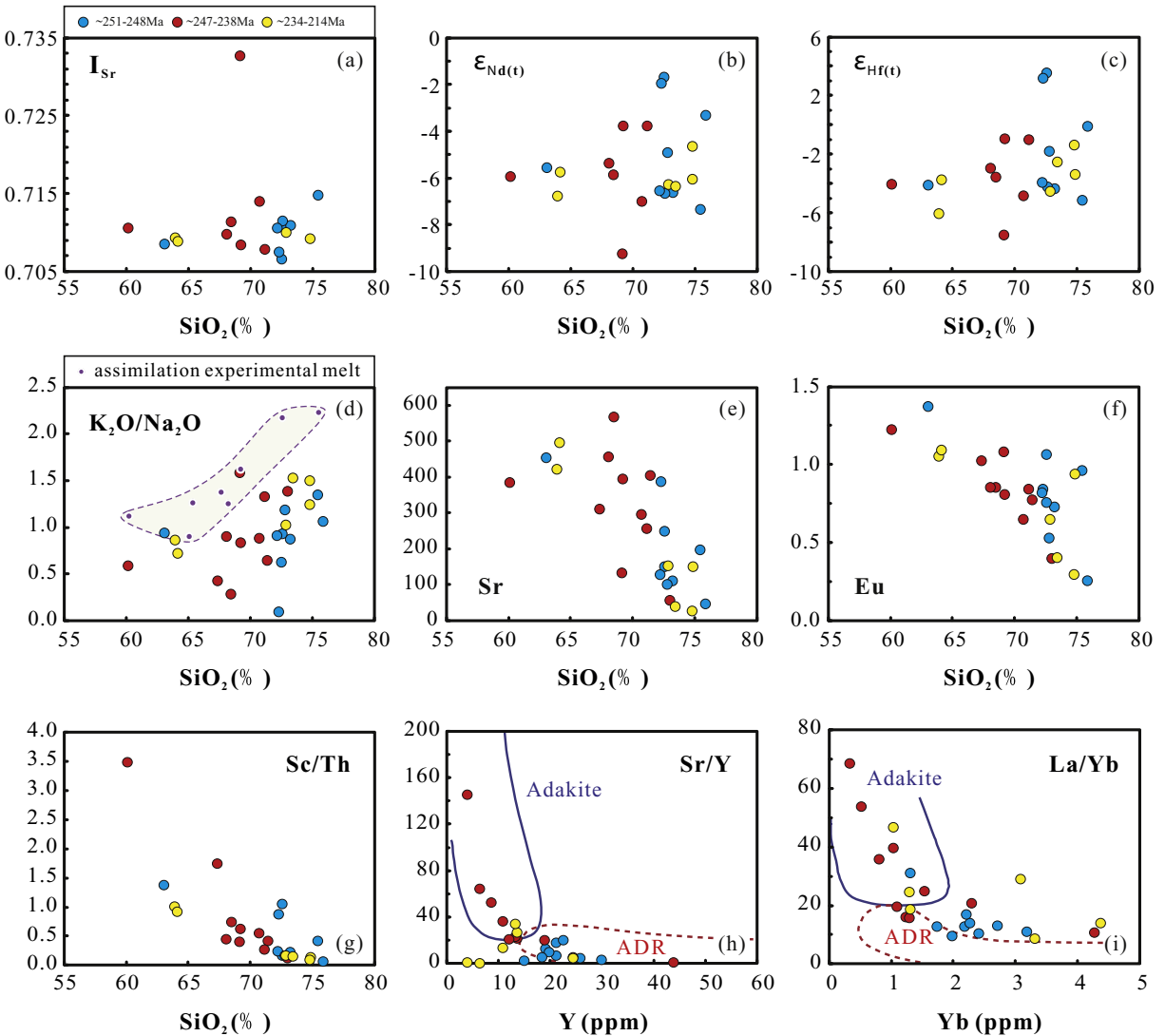


Fig. 7. SiO_2 variation diagrams of (a) I_{Sr} , (b) $\varepsilon_{\text{Nd}(\text{t})}$, (c) $\varepsilon_{\text{Hf}(\text{t})}$, (d) $\text{K}_2\text{O}/\text{Na}_2\text{O}$ (purple filled circles restricted in the purple dash line are products of the assimilation experiments that simulate the reaction between basalts and felsic pelitic gneiss in the crust; Castro, 2001), (e) Sr, (f) Eu and (g) Sc/Th for the Triassic granitoids from the East Kunlun Orogenic Belt. Plots of (h) Sr/Y vs. Y and (i) La/Yb vs. Yb for these samples are used to distinguish adakitic rocks from normal arc andesite, dacite and rhyolite (Castillo, 2012). (For interpretation of the references to colour in this figure legend, the reader is referred to the web version of this article.)

the bulk continental crust with almost identical Nb-Ta-Ti and Sr and Eu depletion (Fig. 6a, d). Secondly, the whole rock Sr-Nd-Hf isotopes can be explained by partial melting of subducted Paleo-Tethyan MORB with terrigenous sediment addition in the melting region under the amphibolite-facies conditions (see above). Though the granitoids in the EKOB have relatively unradiogenic Nd isotope ($\varepsilon_{\text{Nd}(\text{t})} < 0$) compared to the LVS, they have high $\varepsilon_{\text{Hf}(\text{t})}$ values (up to 3.59), which is the more convincing evidence that they are juvenile crust newly formed from ocean crust melting with inherited mantle isotopic signatures and crustal/sediment contribution.

5.2.2. Petrogenesis of the middle (~247–238 Ma) and late Triassic (~234–214 Ma) granitoids

Since the middle Triassic (T_2 , ~247–238 Ma) and late Triassic (T_3 , ~234–214 Ma) granitoids display similar trace elemental and isotopic features (Figs. 6–10), we hence discuss them together here. The T_2 and T_3 granitoids have almost consistent mean values of $\varepsilon_{\text{Nd}(\text{t})}$ (−5.83 [T_2], −5.97 [T_3]) and $\varepsilon_{\text{Hf}(\text{t})}$ (−3.52 [T_2], −3.58 [T_3])), indicating a similar source. REE patterns of the T_2 and T_3 granitoids show weakly concave upward between middle and heavy REEs (Fig. 6b–c), suggesting amphibole as a residual phase in the source due to its high partition

coefficients for middle to heavy REEs, especially the highest $D(\text{Dy})$ in intermediate to felsic melts (Rollinson, 1993). Meanwhile, the multi-element patterns of the T_2 and T_3 granitoids show obvious decrease from Dy to Yb (Fig. 6e–f), which imply garnet may also be a residual phase in their source ($K_{\text{d}}^{\text{Grt/L}} = 39.9$; Arth, 1976). The existence of garnet as a residual phase may be responsible for the adakitic signature (Castillo, 2012) of the T_2 and T_3 granitoids. Most of the T_2 and T_3 granitoids have relatively high Sr/Y and La/Yb , plotting in the field restricted to adakite (Figs. 7h–i). Petrogenesis of adakitic rocks are considered as follows: (1) related to the melting of subducted slab directly or indirectly (Martin et al., 2005); (2) melting of the mafic lower continental crust (e.g. Atherton and Petford, 1993; Goss and Kay, 2009); (3) high pressure fractionation of garnet-bearing normal arc magma (Macpherson et al., 2006). Their high $^{87}\text{Sr}/^{86}\text{Sr}$ (0.7107–0.7523), low $^{143}\text{Nd}/^{144}\text{Nd}$ (0.5120–0.5123) are not a typical signature of melting of subducted slab (Castillo, 2012). Considering the lithostratigraphic records, these granitoids cannot be interpreted as product of arc magmatism (Jiang et al., 1992). Therefore, partial melting of the lower continental crust may account for the origin of the granitic rock. First, the T_2 and T_3 granitoids from the EKOB have high $(\text{La}/\text{Yb})_{\text{N}}$ (Fig. 6b,c) and high $\text{K}_2\text{O}/\text{Na}_2\text{O}$ ratios (Fig. 7d), which are consistent with the

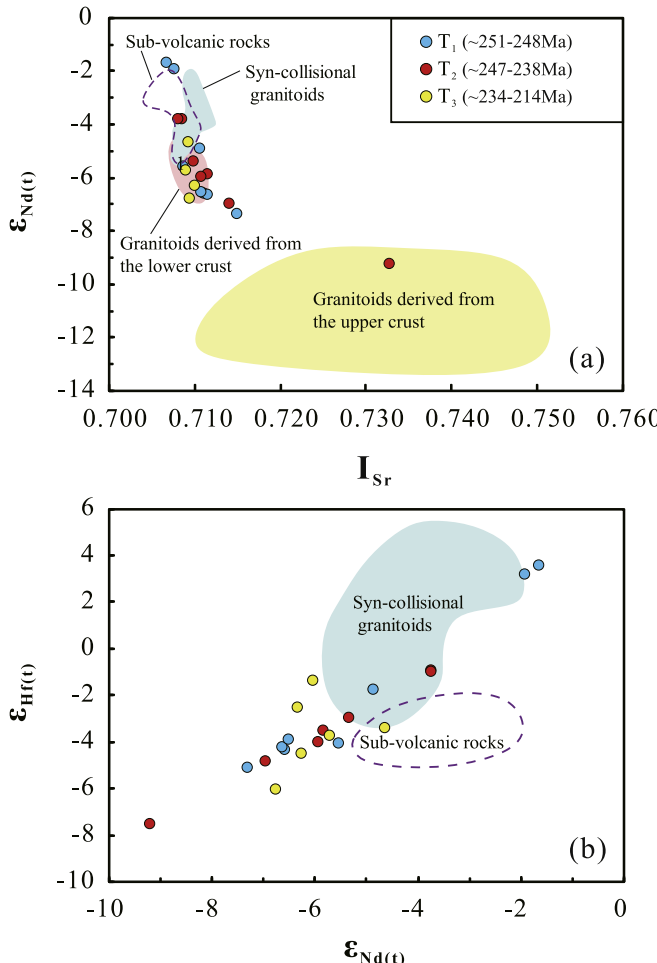


Fig. 8. Diagrams of $\epsilon_{\text{Nd}(t)}$ vs. I_{Sr} (a) and $\epsilon_{\text{Hf}(t)}$ vs. $\epsilon_{\text{Nd}(t)}$ for the Triassic granitoids from the East Kunlun Orogenic Belt. The field of I-type syn-collisional granitoids derived from subducted oceanic crust is based on Huang et al. (2014) and Zhang et al. (2016). The data for the sub-volcanic rocks derived from crust-mantle mixing are from Ding et al. (2011) and Hu et al. (2016). And the I-type granitoids derived from the lower crust and S-type granitoids derived from the upper crust are from Zhang et al. (2012) and Ba et al. (2012), respectively.

composition of adakitic rocks inferred to be derived from partial melting of the lower continental crust. Second, the T_2 and T_3 granitoids from the EKOB have Sr ($^{87}\text{Sr}/^{86}\text{Sr}$, 0.7107–0.7523), Nd ($\epsilon_{\text{Nd}(t)}$, −5.83 [T_2], −5.97 [T_3]) and Hf ($\epsilon_{\text{Hf}(t)}$, −3.52 [T_2], −3.58 [T_3]) isotopes similar to the T_1 granitoids (Figs. 8, 9), are likely indicative of significant juvenile mafic continental crust. Meanwhile, according to the mass balance, the T_2 and T_3 granitoids require some input of mature crustal material (Fig. 10b). Finally, the overlapping Sr-Nd-Hf isotope compositions of the T_2 and T_3 granitoids are consistent with the I-type granitoids derived from the lower continental crust as well as the sub-volcanic rocks derived from crust-mantle mixing (Fig. 8; Zhang et al., 2012; Ding et al., 2011; Hu et al., 2016), which also suggest the T_2 and T_3 granitoids could be produced by melting of the juvenile mafic lower continental crust, mixing with the upper continental crust components during ascent. In which a newly lower crust thickened (probably ~50 km with lowest temperature gradient of $20^{\circ}\text{C km}^{-1}$; Atherton and Petford, 1993) by underplating under garnet stability conditions played an important role, resulting in adakitic features of the T_2 and T_3 granitoids. They likely experienced fractional crystallization of plagioclase (Figs. 5b, e; 7e–f). Furthermore, high partition coefficient of Sc but low value of Th in biotite will result in lower Sc/Th of residual melts during biotite fractionation (Bea et al.,

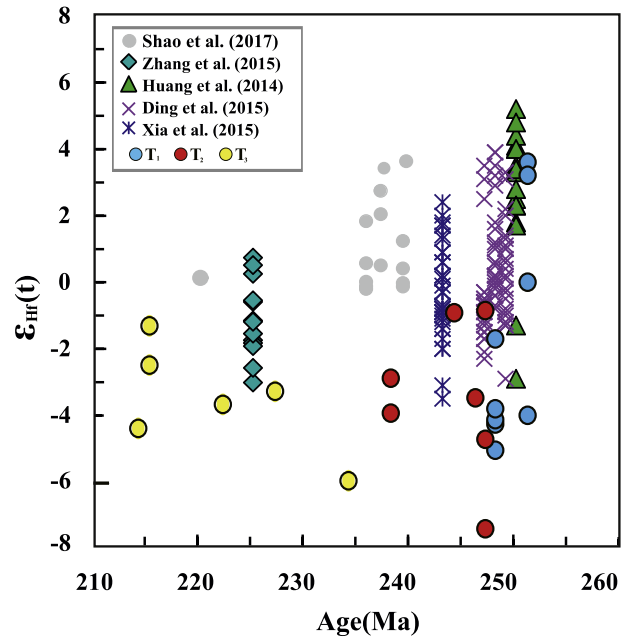


Fig. 9. The $\epsilon_{\text{Hf}(t)}$ vs. Ages of the Triassic granitoids of the East Kunlun orogenic belt. Our new data and the literature data are indicated as the following: light blue diamonds (whole rock Hf data, West Kunlun; Zhang et al., 2016); green triangles (whole rock Hf data, East Kunlun; Huang et al., 2014); purple crosses and blue crosses (zircon Hf data, East Kunlun; Ding et al., 2015; Xia et al., 2015) and gay circles (whole rock Hf data, East Kunlun; Shao et al., 2017). (For interpretation of the references to colour in this figure legend, the reader is referred to the web version of this article.)

1994). Negative correlation between Sc/Th and SiO₂ denotes the biotite fractionation in T_2 and T_3 granitoids (Fig. 7g). In fact, melting the lower crust clearly need a heat source from below. Post-collisional setting of the late Triassic has been widely accepted in the EKOB (e.g. Pan et al., 2012; Wang et al., 2014a). Many mechanisms such as mantle plume (Chung and Jahn, 1995), slab break-off (Maury et al., 2000) or convective lithosphere removal (Hoernle et al., 2006) can cause asthenospheric upwelling, decompression melting, triggering crustal melting. Accordingly, we prefer the more reasonable post-collisional extension and related orogenic collapse for inducing asthenosphere upwelling, and then leading to mafic lower crust melting to form T_2 and T_3 granitoids. The age range of the T_3 granitoids (~234–214 Ma) are similar to the late Triassic mafic dikes and felsic volcanic rocks (228–218 Ma) associated with post-collisional extension in the EKOB (Hu et al., 2016) suggest these post-collisional magmatism is an important tectono-magmatic event which has influenced both the lower crust and the upper mantle. More importantly, the identical genetic link between T_2 and T_3 granitoids has pushed this event back to ~247 Ma, that is the EKOB had transformed to post-collisional setting since the middle Triassic (~247 Ma).

5.3. An integrated model from syn-collisional to post-collisional settings

Our integrate model implies a process of partial melting of the subducted A'nyemaqen ocean crust with terrestrial sediments in a syn-collisional setting (~251–248 Ma) and partial melting of juvenile mafic lower crust mixing with the upper crust components in a post-collisional setting (~247–214 Ma). Fig. 10 shows mixing calculations for the Triassic granitoids in the EKOB. The T_1 (~251–248 Ma) granitoids represent mixing of at least ~50% A'nyemaqen MORB (Guo et al., 2007) and ~50% terrigenous sediments represented by the Jinshuihou granites derived from the Proterozoic basement of Qaidam terrane (Yu et al.,

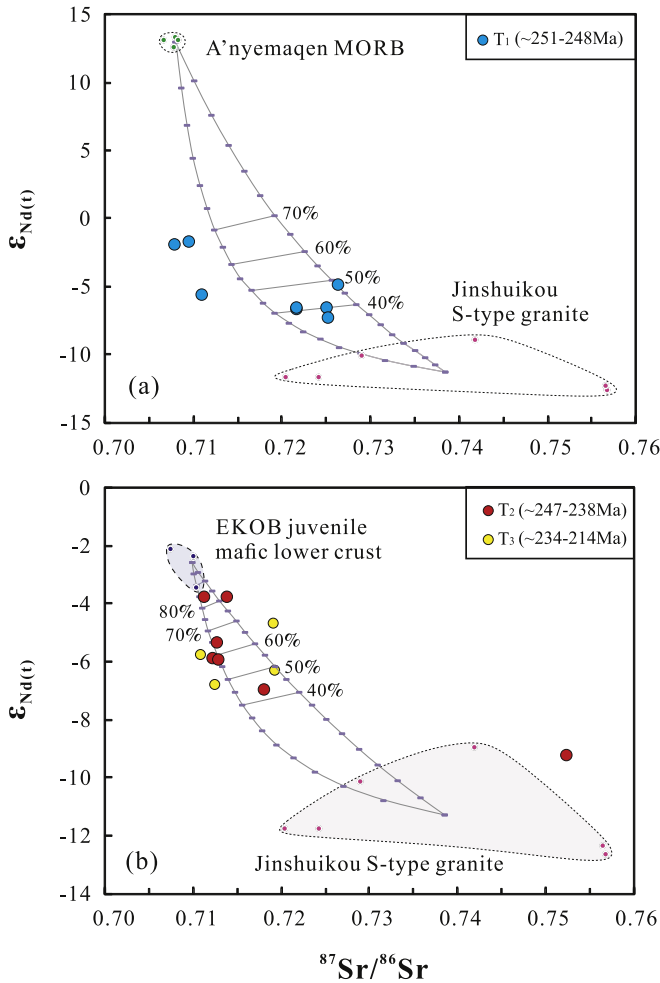


Fig. 10. Mixing trends calculated with $\epsilon_{\text{Nd}(t)}$ and $^{87}\text{Sr}/^{86}\text{Sr}$ composition for (a) the early (~251–248 Ma) and (b) middle (~247–238 Ma) & late (~234–214 Ma) Triassic granitoids from the East Kunlun Orogenic Belt. T_1 granitoids could be explained by mixing between A'nyemaqen MORB (average composition: $^{87}\text{Sr}/^{86}\text{Sr} = 0.707818$, $\epsilon_{\text{Nd}(t)} = 12.9$, Sr = 191.5 ppm, Nd = 8.9 ppm) (Guo et al., 2007) and terrigenous sediments (represented by the Jinshuijou S-type granites) (average composition: $^{87}\text{Sr}/^{86}\text{Sr} = 0.738282$, $\epsilon_{\text{Nd}(t)} = -11.3$, Sr = 260.1 ppm, Nd = 23.3 ppm) (Yu et al., 2005). Comparably, T_2 & T_3 granitoids could be interpreted as mixture of Juvenile mafic lower continental crust (average composition: $^{87}\text{Sr}/^{86}\text{Sr} = 0.709589$, $\epsilon_{\text{Nd}(t)} = -2.6$, Sr = 525.0 ppm, Nd = 33.2 ppm) (Hu et al., 2016) and upper continental crust (represented by the Jinshuijou S-type granites again).

2005). Comparably, the T_2 (~247–238 Ma) and T_3 (~234–214 Ma) granitoids are best explained as hybrid magmas of ~55% juvenile mafic lower crust (Hu et al., 2016) and ~45% upper continental crust materials (also logically represented by the Jinshuijou granitoids; Yu et al., 2005). Melting of A'nyemaqen ocean crust fragments with recycled terrigenous sediment under amphibolite facies conditions resulted in the T_1 granitoids with mantle signatures (e.g. $\epsilon_{\text{Hf}(t)} > 0$), which share similar compositions with the BCC. This process added a net flux of juvenile dioritic to granitic materials to the continental crust, pointing to the significance of the oceanic crust melting for continental crust accretion (Fig. 11a). T_2 and T_3 granitoids are associated with post-collisional magmatism involving participation of juvenile continental crust. Asthenosphere upwelling and decompression melting would provide heat for juvenile mafic lower crust melting, then mixing with upper crust during post-collisional extension (Fig. 11b). These hypotheses are conceptually important for understanding the origin of the juvenile crust and continental crustal growth through magmatism from syn-collisional to post-collisional settings. Further research is needed to test these hypotheses.

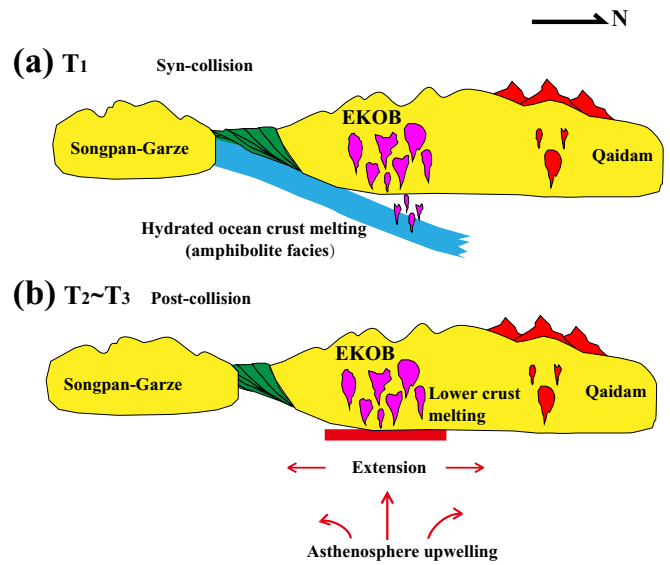


Fig. 11. Schematic illustration for the generation of the granitoids in EKOB during the Triassic (modified from Shao et al., 2017). See text for explanation.

6. Conclusion

1. The zircon U–Pb dating yields ages of ~251–248 Ma, ~247–238 Ma to ~234–214 Ma for the granitoids of the East Kunlun Orogenic Belt. These age data, together with the literature data, suggest that the granitoids are products of syn-collisional (~251–248 Ma) and post-collisional (~247–238 Ma to ~234–214 Ma) magmatism during or shortly after the closure of the A'nyemaqen Ocean.
2. The early Triassic (~251–248 Ma) granitoids are best explained by partial melting of the subducted A'nyemaqen ocean crust fragments with recycled terrigenous sediment under amphibolite facies conditions. The contribution of the ocean crust at least ~50% to the parental melts of the T_1 granitoids, which subsequently underwent fractionation.
3. The middle (~247–238 Ma) and late (~234–214 Ma) Triassic granitoids with adakitic features could be produced by melting of the juvenile mafic lower continental crust, mixing with the upper continental crust components during ascent, in which the relative proportion of juvenile mafic lower crust may be up to ~55% to their parental melts. This process is more reasonably associated with post-collisional extension for inducing asthenosphere upwelling, leading to mafic lower crust melting to form the granitoids.
4. The early Triassic (~251–248 Ma) granitoids with mantle signatures (e.g. $\epsilon_{\text{Hf}(t)} > 0$) as well as BCC-like compositions represent a net flux of juvenile dioritic to granitic materials adding to the continental crust, pointing to the significance of melting of ocean crust for continental crust accretion in the EKOB. And the identical genetic link between T_2 (~247–238 Ma) and T_3 (~234–214 Ma) granitoids means the EKOB had transformed to post-collisional setting since the middle Triassic (~247 Ma).

Acknowledgements

We thank Pengyuan Guo, Pu Sun, Zhenxing Hu, Jinju Liu and Huixia Cui for help in the field, and Lian Zhou for assistance with isotope analysis. We also thank Professor Michael Roden and two anonymous reviewers for their constructive comments and suggestions on the manuscript improvement. This work was supported by grants from Chinese Academy of Sciences, regional and local authorities (Shandong Province and Qingdao, U1606401), Natural Foundation of

Shandong Province (ZR2018BD020), Qingdao National laboratory of ocean sciences and Technology (2015ASKJ03) and National Natural Science Foundation of China (41630968, 91014003, 41803028, 91958215) and the 111 Project of China (B118048).

Declaration of Interest Statement

No potential conflict of interest was reported by the authors.

Appendix A. Supplementary data

References

- Atherton, M.P., Petford, N., 1993. Generation of sodium-rich magmas from newly underplated basaltic crust. *Nature* 362, 144–146.
- Ba, J., Chen, N.S., Wang, Q.Y., Wang, X.Y., Zhang, L., Wang, S.Q., 2012. Nd-Sr-Pb isotopic compositions of cordierite granite on southern margin of the qaidam block, NW China, and constraints on its petrogenesis, tectonic affinity of source region and tectonic implications. *Earth Sci. J. China Univer. Geosci.* 80–92.
- Bea, F., Pereira, M.D., Stroh, A., 1994. Mineral/leucosome trace-element partitioning in a peraluminous migmatite (a laser ablation-ICP-MS study). *Chem. Geol.* 117, 291–312.
- Bian, Q.T., Li, D.H., Pospelov, I., Yin, L.M., Li, H.S., Zhao, D.S., Chang, C.F., Luo, X.Q., Gao, S.L., Astrakhantsev, O., 2004. Age, geochemistry and tectonic setting of Buqingshan ophiolites, north Qinghai-Tibet Plateau, China. *J. Asian Earth Sci.* 23, 577–596.
- Bian, Q.T., Yin, L.M., Sun, S.F., Luo, X.Q., Pospelov, I., Astrakhantsev, O., Chamov, N., 2001. Discovery of Ordovician acritarchs in Buqingshan ophiolite complex, East Kunlun Mountains and its significance. *Chin. Sci. Bull.* 46, 341–345.
- Castillo, P.R., 2012. Adakite petrogenesis. *Lithos* 134, 304–316.
- Castro, A., 2001. Plagioclase morphologies in assimilation experiments. Implications for disequilibrium melting in the generation of granodiorite rocks. *Mineral. Petrol.* 71, 31–49.
- Castro, A., Gerya, T., García-Casco, A., Fernández, C., Díaz-Alvarado, J., Moreno-Ventas, I., Löw, I., 2010. Melting relations of MORB-sediment mélanges in underplated mantle wedge plumes; implications for the origin of cordilleran-type batholiths. *J. Petrol.* 51, 1267–1295.
- Chappell, B.W., White, A.J.R., 2001. Two contrasting granite types: 25 years later. *Aust. J. Earth Sci.* 48, 489–499.
- Chen, B., Arakawa, Y., 2005. Elemental and Nd-Sr isotopic geochemistry of granitoids from the West Junggar foldbelt (NW China), with implications for Phanerozoic continental growth. *Geochim. Cosmochim. Acta* 69, 1307–1320.
- Chen, N.S., Sun, M., Wang, Q.Y., Zhao, G.C., Chen, Q., Shu, G.M., 2007. EMP chemical ages of monazites from Central Zone of the eastern Kunlun Orogen: Records of multi-tectonometamorphic events. *Chin. Sci. Bull.* 52, 2252–2263.
- Chen, Y.X., Pei, X.Z., Li, R.B., Liu, Z.Q., Li, Z.C., Zhang, X.F., Chen, G.C., Liu, Z.G., Ding, S.P., Guo, J.F., 2011. Zircon U-Pb age of Xiaomiao Formation of Proterozoic in the eastern section of the East Kunlun Orogenic Belt. *Geoscience* 25, 510–521.
- Chung, S.L., Jahn, B.M., 1995. Plume-lithosphere interaction in generation of the Emeishan flood basalts at the Permian-Triassic boundary. *Geology* 23, 889–892.
- Collins, W., Beams, S., White, A., Chappell, B., 1982. Nature and origin of A-type granites with particular reference to southeastern Australia. *Contrib. Mineral. Petrol.* 80, 189–200.
- Corfu, F., Hanchar, J.M., Hoskin, P.W.O., Kinny, P., 2003. *Atlas of Zircon Textures*. Rev. Mineral. Geochem. 53, 469–500.
- De Souza, Z.S., Martin, H., Peucat, J.-J., De Sá, E.F.J., Macedo, M.H.D.F., 2007. Calc-alkaline magmatism at the Archean-Proterozoic transition: the Caicó complex Basement (NE Brazil). *J. Petrol.* 48, 2149–2185.
- Ding, S., Huang, H., Niu, Y.L., Zhao, Z.D., Yu, X.H., Mo, X.X., 2011. Geochemistry, geochronology and petrogenesis of East Kunlun high Nb-Ta rhyolites. *Acta Petrol. Sin.* 27, 3603–3614.
- Ding, Q.F., Jiang, S.Y., Sun, F.Y., 2014. Zircon U-Pb geochronology, geochemical and Sr-Nd-Hf isotopic compositions of the Triassic granite and diorite dikes from the Wulonggou mining area in the Eastern Kunlun Orogen, NW China: Petrogenesis and tectonic implications. *Lithos* 205, 266–283.
- Ding, Q., Liu, F., Yan, W., 2015. Zircon U-Pb geochronology and Hf isotopic constraints on the petrogenesis of early Triassic granites in the Wulonggou area of the Eastern Kunlun Orogen, Northwest China. *Int. Geol. Rev.* 57, 1735–1754.
- Dong, Y.P., Zhang, G.W., Neubauer, F., Liu, X.M., Hauzenberger, C., Zhou, D.W., Li, W., 2011. Syn-and post-collisional granitoids in the Central Tianshan orogen: geochemistry, geochronology and implications for tectonic evolution. *Gondwana Res.* 20, 568–581.
- Frost, B.R., Barnes, C.G., Collins, W.J., Arculus, R.J., Ellis, D.J., Frost, C.D., 2001. A geochemical classification for granitic rocks. *J. Petrol.* 42, 2033–2048.
- Gao, S., Rudnick, R.L., Yuan, H.L., Liu, X.M., Liu, Y.S., Xu, W.L., Ling, W.L., Ayers, J., Wang, X.C., Wang, Q.H., 2004. Recycling lower continental crust in the North China craton. *Nature* 432, 892–897.
- Goss, A.R., Kay, S.M., 2009. Extreme high field strength element (HFSE) depletion and near-chondritic Nb/Ta ratios in Central Andean adakite-like lavas (-28° S, -68° W). *Earth Planet. Sci. Lett.* 279, 97–109.
- Guo, A.L., Zhang, G.W., Sun, Y.G., Cheng, S.Y., Qiang, J., 2007. Sr-Nd-Pb isotopic geochemistry of late-Paleozoic mafic volcanic rocks in the surrounding areas of the Gonghe basin, Qinghai province and geological implications. *Acta Petrol. Sin.* 23,
- Hoernle, K., White, J.D.L., van den Bogaard, P., Hauff, F., Coombs, D.S., Werner, R., Timm, C., Garbe-Schönberg, D., Reay, A., Cooper, A.F., 2006. Cenozoic intraplate volcanism on New Zealand: Upwelling induced by lithospheric removal. *Earth Planet. Sci. Lett.* 248, 350–367.
- Hoskin, P.W.O., Schaltegger, U., 2003. The Composition of Zircon and Igneous and Metamorphic Petrogenesis. Mineralogical Society of America, Washington, DC, ETATS-UNIS, p. 36.
- Hu, Y., Niu, Y.L., Li, J.Y., Ye, L., Kong, J.J., Chen, S., Zhang, Y., Zhang, G.R., 2016. Petrogenesis and tectonic significance of the late Triassic mafic dikes and felsic volcanic rocks in the East Kunlun Orogenic Belt, Northern Tibet Plateau. *Lithos* 245, 205–222.
- Huang, H., Niu, Y.L., Nowell, G., Zhao, Z.D., Yu, X.H., Zhu, D.C., Mo, X.X., Ding, S., 2014. Geochemical constraints on the petrogenesis of granitoids in the East Kunlun Orogenic belt, northern Tibetan Plateau: Implications for continental crust growth through syn-collisional felsic magmatism. *Chem. Geol.* 370, 1–18.
- Jiang, C.F., Yang, J.S., Feng, B.G., Zhu, Z.Z., Zhao, M., Chai, Y.C., Shi, X.D., Wang, H.D., Hu, J.Q., 1992. Opening-closing tectonics of Kunlun Mountains. *Ser. Geol. Mem.* 5, 1–224.
- Kong, J.J., Niu, Y.L., Duan, M., Zhang, Y., Hu, Y., Li, J.Y., Chen, S., 2017. Petrogenesis of Luchuba and Wuchaba granitoids in western Qinling: Geochronology and geochemical evidence. *Mineral. Petrol.* 111, 887–908.
- Laurent, A., Janoušek, V., Magna, T., Schulmann, K., Miková, J., 2014. Petrogenesis and geochronology of a post-orogenic calc-alkaline magmatic association: the Žulová Pluton, Bohemian Massif. *J. GEOSciences* 415–440.
- Li, L., Dong, F.C., Yang, Y.Q., Zhu, Z.X., Jiang, H.B., Xin, J., 2012. The Petrology and Geochemistry of Ophiolites from Central Kunlun. *Xinjiang Geol.* 30, 19–25.
- Liu, C.D., Mo, X.X., Luo, Z.H., Yu, X.H., Chen, H.W., Li, S.W., Zhao, X., 2004. Mixing events between the crust- and mantle-derived magmas in eastern kunlun: evidence from zircon SHRIMP II chronology. *Chin. Sci. Bull.* 49, 828–834.
- Liu, Y.S., Hu, Z.C., Zong, K.Q., Gao, C.G., Gao, S., Xu, J., Chen, H.H., 2010. Reappraisal and refinement of zircon U-Pb isotope and trace element analyses by LA-ICP-MS. *Chin. Sci. Bull.* 55, 1535–1546.
- Liu, Z., Jiang, Y.H., Jia, R.Y., Zhao, P., Zhou, Q., 2015. Origin of late Triassic high-K calc-alkaline granitoids and their potassio microgranular enclaves from the western Tibet Plateau, Northwest China: Implications for Paleo-Tethys evolution. *Gondwana Res.* 27, 326–341.
- Ludwig, K.R., 2012. User's manual for Isoplot version 3.75–4.15: a geochronological toolkit for Microsoft Excel Berkley Geochronological Center Special Publication, No.5.
- Luo, B.J., Zhang, H.F., Xu, W.C., Guo, L., Pan, F.B., Yang, H., 2015. The Middle Triassic Meiwu Batholith, West Qinling, Central China: Implications for the Evolution of Compositional Diversity in a Composite Batholith. *J. Petrol.* 56 (6), 1139–1172.
- Macpherson, C.G., Dreher, S.T., Thirlwall, M.F., 2006. Adakites without slab melting: high pressure differentiation of island arc magma, Mindanao, the Philippines. *Earth Planet. Sci. Lett.* 243, 581–593.
- Maniar, P.D., Piccoli, P.M., 1989. Tectonic discrimination of granitoids. *Geol. Soc. Am. Bull.* 101, 635–643.
- Martin, H., Smithies, R.H., Rapp, R., Moyen, J.F., Champion, D., 2005. An overview of adakite, tonalite-trondhjemite-granodiorite (TTG), and sanukitoid: relationships and some implications for crustal evolution. *Lithos* 79, 1–24.
- Maury, R.C., Fourcade, S., Coulon, C., Bellon, H., Coutelle, A., Ouabadi, A., Semroud, B., Megartsi, M.h., Cotten, J., Belanteur, O., 2000. Post-collisional Neogene magmatism of the Mediterranean Maghreb margin: a consequence of slab breakup. *Comptes Rendus de l'Académie des Sciences-Series IIA-Earth and Planetary Science* 331, 159–173.
- Middlemost, E.A., 1994. Naming materials in the magma/igneous rock system. *Earth-Sci. Rev.* 37, 215–224.
- Mo, X.X., Luo, Z.H., Deng, J.F., Yu, X.H., Liu, C.D., Chen, H.W., Yuan, W.M., Liu, Y.H., 2007. Granitoids and Crustal Growth in the East-Kunlun Orogenic Belt. *Geol. J. China Univ.* 13, 403–414.
- Mo, X.X., Niu, Y.L., Dong, G.C., Zhao, Z.D., Hou, Z.Q., Zhou, S., Ke, S., 2008. Contribution of syncollisional felsic magmatism to continental crust growth: a case study of the Paleogene Linzizong volcanic succession in southern Tibet. *Chem. Geol.* 250, 49–67.
- Niu, Y.L., O'Hara, M.J., 2009. MORB mantle hosts the missing Eu (Sr, Nb, Ta and Ti) in the continental crust: New perspectives on crustal growth, crust-mantle differentiation and chemical structure of oceanic upper mantle. *Lithos* 112, 1–17.
- Niu, Y.L., Zhao, Z.D., Zhu, D.C., Mo, X.X., 2013. Continental collision zones are primary sites for net continental crust growth – a testable hypothesis. *Earth-Sci. Rev.* 127, 96–110.
- Pan, G.T., Wang, L.Q., Li, R.S., Yuan, S.H., Ji, W.H., Yin, F.G., Zhang, W.P., Wang, B.D., 2012. Tectonic evolution of the Qinghai-Tibet Plateau. *J. Asian Earth Sci.* 53, 3–14.
- Ramos, F.C., Reid, M.R., 2005. Distinguishing melting of heterogeneous mantle sources from crustal contamination: insights from Sr isotopes at the Phenocryst Scale, Pisgah Crater, California. *J. Petrol.* 46, 999–1012.
- Rickwood, P.C., 1989. Boundary lines within petrologic diagrams which use oxides of major and minor elements. *Lithos* 22, 247–263.
- Rollinson, H., 1993. Using Geochemical Data: Evaluation, Interpretation, Presentation. Longman, New York.
- Rudnick, R.L., Gao, S., 2003. Composition of the continental crust. *Treatise Geochem.* 3, 1–64.
- Shao, F.L., Niu, Y.L., Regelous, M., Zhu, D.C., 2015. Petrogenesis of peralkaline rhyolites in an intra-plate setting: Glass House Mountains, Southeast Queensland, Australia. *Lithos* 216, 196–210.
- Shao, F., Niu, Y., Liu, Y., Chen, S., Kong, J., Duan, M., 2017. Petrogenesis of triassic granitoids in the east kunlun orogenic belt, northern tibetan plateau and their tectonic implications. *Lithos* 282–283, 33–44.
- Song, S.G., Su, L., Li, X.H., Zhang, G.B., Niu, Y.L., Zhang, L.F., 2010. Tracing the 850-Ma continental flood basalts from a piece of subducted continental crust in the North Qaidam UHPM belt, NW China. *Precambrian Res.* 183, 805–816.

- Sun, S.-s., McDonough, W.F., 1989. Chemical and isotopic systematics of oceanic basalts: implications for mantle composition and processes. *Geol. Soc. Lond. Spec. Publ.* 42, 313–345.
- Sun, Y., Pei, X.Z., Ding, S.P., Li, R.B., Feng, J.Y., Zhang, Y.F., Li, Z.C., Chen, Y.X., Zhang, X.F., Chen, G.C., 2009. Halagatu magma mixing granite in the East Kunlun Mountains—evidence from Zircon U-Pb dating. *Acta Geol. Sin.* 83, 1000–1010.
- Taylor, S.R., 1967. The origin and growth of continents. *Tectonophysics* 4, 17–34.
- Wang, G.C., Wang, Q.H., Ran, P., Zhu, Y.H., 2004. Zircon SHRIMP ages of Precambrian metamorphic basement rocks and their tectonic significance in the eastern Kunlun Mountains, Qinghai Province, China. *Dixue Qianyuan (Earth Science Frontiers)* 11, 481–490.
- Wang, G.C., Wei, Q.R., Jia, C.X., Zhang, K.X., Li, D.W., Zhu, Y.H., Xiang, S.Y., 2007. Some ideas of Precambrian geology in the East Kunlun, China. *Geol. Bull. China* 26, 929–937.
- Wang, B.Z., Chen, J., Luo, Z.H., Chen, F.B., Wang, T., Guo, G.E., 2014a. Spatial and temporal distribution of late Permian-early Jurassic intrusion assemblages in eastern Qimantag, East Kunlun, and their tectonic settings. *Acta Petrol. Sin.* 30, 3213–3228.
- Whalen, J.B., Currie, K.L., Chappell, B.W., 1987. A-type granites: geochemical characteristics, discrimination and petrogenesis. *Contrib. Mineral. Petro.* 95, 407–419.
- Wiedenbeck, M., Alle, P., Corfu, F., Griffin, W.L., Meier, M., Oberli, F., Quadtt, A.v., Roddick, J.C., Spiegel, W., 1995. Three natural zircon standards for U-Th-Pb, Lu-Hf, trace element and REE analyses. *Geostand. Newslett.* 19, 1–23.
- Wu, F.Y., Jahn, B.M., Wilde, S., Sun, D.Y., 2000. Phanerozoic crustal growth: U-Pb and Sr-Nd isotopic evidence from the granites in northeastern China. *Tectonophysics* 328, 89–113.
- XACGS, 2009. Geological Map of Kunlun Mountain and its Adjacent Area, Scale 1: 1000,000. Xi'an Center of Geological Survey, China Geological Survey.
- Xia, R., Wang, C., Qing, M., Li, W., Carranza, E.J.M., Guo, X., Ge, L., Zeng, G., 2015. Zircon U-Pb dating, geochemistry and Sr-Nd-Pb-Hf-O isotopes for the Nan'getan granodiorites and mafic microgranular enclaves in the East Kunlun orogen: record of closure of the Paleo-Tethys. *Lithos* 234–235, 47–60.
- Xiong, F.H., Ma, C.Q., Zhang, J.Y., Liu, B., 2012. The origin of mafic microgranular enclaves and their host granodiorites from East Kunlun, Northern Qinghai-Tibet Plateau: implications for magma mixing during subduction of Paleo-Tethyan lithosphere. *Mineral. Petroil.* 104, 211–224.
- Xiong, F.H., Ma, C.Q., Jiang, H.A., Liu, B., Huang, J., 2014. Geochronology and geochemistry of Middle Devonian mafic dykes in the East Kunlun orogenic belt, Northern Tibet Plateau: Implications for the transition from Prototethys to Paleotethys orogeny. *Chem. Erde-Geochem.* 74, 225–235.
- Xu, Z.Q., Dilek, Y., Cao, H., Yang, J.S., Robinson, P., Ma, C.Q., Li, H.Q., Jolivet, M., Roger, F., Chen, X.J., 2015. Paleo-Tethyan Evolution of Tibet as Recorded in the East Cimmerides and West Cathaysides. *J. Asian Earth Sci.* 105, 320–337.
- Yang, J.S., Robinson, P.T., Jiang, C.F., Xu, Z.Q., 1996. Ophiolites of the Kunlun Mountains, China and their tectonic implications. *Tectonophysics* 258, 215–231.
- Yang, J.S., Shi, R.D., Wu, C.L., Wang, X.B., Robinson, P., 2009. Dur'ngoi ophiolite in East Kunlun, Northeast Tibetan plateau: Evidence for paleo-Tethyan suture in Northwest China. *J. Earth Sci.* 20, 303–331.
- Yang, Y.H., Zhang, H.F., Chu, Z.Y., Xie, L.W., Wu, F.Y., 2010b. Combined chemical separation of Lu, Hf, Rb, Sr, Sm and Nd from a single rock digest and precise and accurate isotope determinations of Lu–Hf, Rb–Sr and Sm–Nd isotope systems using Multi-Collector ICP-MS and TIMS. *Int. J. Mass Spectrom.* 290, 120–126.
- Yu, N., Jin, W., Ge, W.C., Long, X.P., 2005. Geochemical study on peraluminous granite from Jinshuihou in East Kunlun. *Global Geol.* 24, 123–128.
- Zhang, J.Y., Ma, C.Q., Xiong, F.H., Liu, B., 2012. Petrogenesis and tectonic significance of the Late Permian–Middle Triassic calc-alkaline granites in the Balong region, eastern Kunlun Orogen, China. *Geol. Mag.* 149, 892–908.
- Zhang, J.Y., Ma, C.Q., Xiong, F.H., Liu, B., Li, J.W., Pan, Y.M., 2014. Early Paleozoic high-Mg diorite–granodiorite in the eastern Kunlun Orogen, western China: Response to continental collision and slab break-off. *Lithos* 210, 129–146.
- Zhang, J.X., Meng, F.C., Wan, Y.S., Yang, J.S., Tung, K.A., 2003. Early Paleozoic tectono-thermal event of the Jingshuikou Group on the south margin of Qaidam: zircon U-Pb SHRIMP age evidence. *Geol. Bull. of China* 22, 397–404.
- Zhang, Y., Niu, Y.L., Hu, Y., Liu, J.J., Ye, L., Kong, J.J., Duan, M., 2016. The syncollisional granitoid magmatism and continental crust growth in the West Kunlun Orogen, China—evidence from geochronology and geochemistry of the Arkarz pluton. *Lithos* 245, 191–204.